

## Aberystwyth University

### *Infrared radiofluorescence (IR-RF) dating*

Murari, Madhav Krishna; Kreutzer, Sebastian; King, Georgina; Frouin, Marine; Tsukamoto, Sumiko; Schmidt, Christoph; Lauer, Tobias; Klasen, Nicole; Richter, Daniel; Friedrich, Johannes; Mercier, Norbert; Fuchs, Markus

*Published in:*

Quaternary Geochronology

*DOI:*

[10.1016/j.quageo.2021.101155](https://doi.org/10.1016/j.quageo.2021.101155)

*Publication date:*

2021

*Citation for published version (APA):*

Murari, M. K., Kreutzer, S., King, G., Frouin, M., Tsukamoto, S., Schmidt, C., Lauer, T., Klasen, N., Richter, D., Friedrich, J., Mercier, N., & Fuchs, M. (2021). Infrared radiofluorescence (IR-RF) dating: A review. *Quaternary Geochronology*, 64, [101155]. <https://doi.org/10.1016/j.quageo.2021.101155>

#### **Document License**

CC BY-NC-ND

#### **General rights**

Copyright and moral rights for the publications made accessible in the Aberystwyth Research Portal (the Institutional Repository) are retained by the authors and/or other copyright owners and it is a condition of accessing publications that users recognise and abide by the legal requirements associated with these rights.

- Users may download and print one copy of any publication from the Aberystwyth Research Portal for the purpose of private study or research.
- You may not further distribute the material or use it for any profit-making activity or commercial gain
- You may freely distribute the URL identifying the publication in the Aberystwyth Research Portal

#### **Take down policy**

If you believe that this document breaches copyright please contact us providing details, and we will remove access to the work immediately and investigate your claim.

tel: +44 1970 62 2400  
email: [is@aber.ac.uk](mailto:is@aber.ac.uk)

# 1 **Infrared Radiofluorescence (IR-RF) dating: a review**

2 Madhav Krishna Murari<sup>1,2</sup>, Sebastian Kreutzer<sup>3,4,\*</sup>, Georgina King<sup>5</sup>, Marine Frouin<sup>6,7</sup>, Sumiko Tsukamoto<sup>8</sup>,  
3 Christoph Schmidt<sup>5,9</sup>, Tobias Lauer<sup>10</sup>, Nicole Klasen<sup>11</sup>, Daniel Richter<sup>10,12</sup>, Johannes Friedrich<sup>9</sup>, Norbert  
4 Mercier<sup>4</sup>, Markus Fuchs<sup>1</sup>

5 <sup>1</sup>Department of Geography, Justus Liebig University, Giessen, Germany

6 <sup>2</sup>Geochronology Project, Inter-University Accelerator Centre, New Delhi, India

7 <sup>3</sup>Geography and Earth Sciences, Aberystwyth University, Aberystwyth, United Kingdom

8 <sup>4</sup>IRAMAT-CRP2A, UMR 5060, CNRS - Université Bordeaux Montaigne, Pessac, France

9 <sup>5</sup>Institute of Earth Surface Dynamics, Université de Lausanne, Lausanne, Switzerland

10 <sup>6</sup>Department of Geosciences, Stony Brook University, Stony Brook, NY, United States

11 <sup>7</sup>Research Laboratory for Archaeology and the History of Art, School of Archaeology, Oxford University,  
12 Oxford, United Kingdom

13 <sup>8</sup>Leibniz Institute for Applied Geophysics, Hannover, Germany

14 <sup>9</sup>Chair of Geomorphology, University of Bayreuth, Bayreuth, Germany

15 <sup>10</sup>Department of Human Evolution, Max Planck Institute for Evolutionary Anthropology, Leipzig, Germany

16 <sup>11</sup>Institute of Geography, University of Cologne, Cologne, Germany

17 <sup>12</sup>Freiberg Instruments GmbH, Freiberg, Germany

18 **\*corresponding author:** [sebastian.kreutzer@aber.ac.uk](mailto:sebastian.kreutzer@aber.ac.uk)

19

20

21

22

23

24 **Abstract**

25 Luminescence dating methods on natural minerals such as quartz and feldspars are indispensable  
26 for establishing chronologies in Quaternary Science. Commonly applied sediment dating methods  
27 are optically stimulated luminescence (OSL) and infrared stimulated luminescence (IRSL). In  
28 1999, Trautmann et al. (1999a, b) proposed a new related technique called infrared  
29 radiofluorescence (IR-RF). IR-RF denotes the infrared luminescence signal resulting from  
30 exposure to ionizing radiation and potentially offers a significant methodological advance  
31 compared to OSL and IRSL regarding luminescence signal stability, dating range and required  
32 measurement time. The method has rarely been applied due to a lack of commercially available  
33 measurement equipment but experienced a revival during the last years. The present article  
34 provides a state-of-the-art overview of the physical background of IR-RF, its challenges,  
35 applications and the potential as a dating method. The paper particularly addresses practical  
36 considerations for applying IR-RF dating, including signal bleachability and saturation behaviour,  
37 and summarizes proposed solutions.

38 **Keywords:** Infrared radiofluorescence; Radioluminescence; Feldspar; Chronology;  
39 Luminescence dating

## 40 **1 Introduction**

41 In the late 1990s, Trautmann et al. (1998) characterized radioluminescence signals, the emission  
42 stimulated by ionizing radiation, from various feldspar specimens to investigate their potential for  
43 dating applications. Focusing first on radiation-induced emissions in the UV and yellow  
44 wavelength range, where luminescence signal increases with radiation dose, they incidentally  
45 observed the opposite for potassium bearing (K-) feldspar specimen such as microcline and  
46 orthoclase: a dose-dependent signal decrease of the emission centred at 854 nm (1.45 eV; based  
47 on peak tail fitting only). Later, Trautmann et al. (1999a, b), Schilles (2002) and Erfurt and  
48 Krbetschek (2003a) determined that the emission peak was centred at 865 nm (1.43 eV).  
49 Trautmann et al. (1998) recognized that this emission energy is similar to the excitation energy  
50 used for infrared stimulated luminescence (IRSL, Hütt et al., 1988) and consequently interpreted  
51 this process as a luminescent transition (trapping) of electrons. Their pioneer work paved the way  
52 to what is known today as infrared radiofluorescence (IR-RF) dating; the method first proposed by  
53 Trautmann et al. (1999a, b) and termed by Erfurt and Krbetschek (2003a, b).  
54 The IR-RF signal is believed to be a direct measure of the fraction of empty electron traps, unlike  
55 conventional luminescence dating methods such as those based on thermoluminescence (TL, cf.  
56 Aitken, 1985a), optically stimulated luminescence (OSL, Huntley et al., 1985; Aitken, 1998) and  
57 infrared stimulated luminescence (IRSL, Hütt et al., 1988), for which the signals are associated  
58 with more complex recombination pathways. Since the IR-RF signal intensity *decreases* with  
59 increasing dose, it can be used for dosimetry and dating purposes. IR-RF may provide advantages  
60 over conventional single aliquot regenerative (SAR, Murray and Wintle, 2000) dose, IRSL dating  
61 methods (e.g., SAR IRSL, Wallinga et al., 2000) or its derivatives deploying higher reading  
62 temperatures (post-IR IRSL, Thomsen et al., 2008; MET-pIRIR, Li and Li, 2011a) in terms of  
63 required measurement time (relatively short protocol, cf. Erfurt and Krbetschek, 2003b), resolution  
64 of the dose-response curve (continuous recording of data points) and dating range (Sec. 7).  
65 Nevertheless, IR-RF as a dating method is still subject to ongoing research, with its general  
66 applicability being questioned (Buylaert et al., 2012). On the contrary, recent technological and  
67 methodological work, e.g., on the optical resetting of the IR-RF signal, and improved routines for  
68 dose estimation have yielded promising results (Frouin, 2014; Frouin et al., 2015, 2017; Huot et  
69 al., 2015; Kreutzer et al., 2017; Murari et al., 2018).

70 This contribution provides an overview of past and recent developments of IR-RF from K-feldspar  
71 as a dating method. We summarize current knowledge on existing models on the origin of IR-RF,  
72 outline commonly applied measurement procedures and equipment, and highlight shortfalls,  
73 challenges and open questions. Understanding what remains unknown may stimulate discussions  
74 and lead to improved experimental designs towards a full establishment of IR-RF as a valuable  
75 chronological tool.

## 76 **2 Origin of the IR-RF signal and relevant models**

77 The 1.43 eV (865 nm) IR-RF emission of K-feldspar (Trautmann et al., 1999a, b; 1.45 eV in  
78 Trautmann et al., 1998, see below for an explanation) has the same energy as the typical excitation  
79 maximum of IRSL (Hütt et al., 1988; Poohton et al. 2002a, b), which led Trautmann et al. (1998)  
80 to suggest that both signals are derived from the same principal electron trap. More recent  
81 observations of infrared photoluminescence (IR-PL; Prasad et al., 2017) seem to support this  
82 hypothesis (see also Kumar et al., 2018). Further studies by Kumar et al. (2020) generally  
83 confirmed this view but extended the understanding by assigning two different defect sites to the  
84 principal trap based on their cathodoluminescence measurements.

85 Trautmann et al. (1999a, b) and Trautmann (2000) proposed a model for the IR-RF emission of  
86 feldspar whereby IR-RF results from the transition of an electron from the conduction band to the  
87 ground state of the IRSL trap through the excited state.

88 Figure 1 illustrates the different electronic transitions associated with IRSL and IR-RF production  
89 in one plot. Please note: Although we compiled different ideas in one figure, our graphical  
90 representation *should not* be considered a new model. In Fig. 1, continuous exposure to ionizing  
91 radiation leads to a constant flow of electrons from the valence band to the conduction band [a],  
92 from which electrons can either recombine radiatively [b] or non-radiatively (not shown for  
93 clarity), or become trapped [c]. As irradiation persists, the IRSL trap [c] becomes filled, resulting  
94 in more electrons recombining radiatively [b], accounting for the observed rise in the ultraviolet  
95 (UV)-RF and visible light (VIS)-RF emissions at higher doses (Trautmann et al., 1999a). However,  
96 this model raises two major questions: (1) why does the IR-RF signal not fully saturate during  
97 laboratory irradiation, resulting in a zero or negligible IR-RF signal, and (2) to bleach, why does  
98 the IR-RF signal require exposure to light of higher energies than IR (e.g., Trautmann et al., 1998,

99 1999a, b; Frouin et al., 2015, 2017), whereas the IRSL signal from the same trap could be  
100 efficiently reset through exposure to infrared light?

101 ***Figure 1***

102 ***(Models)***

103 To explain why the IR-RF signal does not appear to saturate, Trautmann et al. (1999a) first  
104 considered electron release throughout irradiation due to the low thermal stability of the IRSL trap,  
105 resulting in the replenishment of free electron-hole pairs and thus a continuously decaying IR-RF  
106 signal. However, this hypothesis contradicts a measured lifetime of the IRSL trap in the range of  
107 Ga (Murray et al., 2009). An alternative explanation not considered by Trautmann et al. (1999a)  
108 is the loss of trapped electrons by athermal tunnelling, known as anomalous fading of feldspar  
109 (e.g., Wintle 1973; Spooner 1992; Visocekas, 1993; Huntley and Lian, 2006) and more  
110 specifically, the anomalous fading of the IRSL feldspar trap (e.g., Spooner 1992; Huntley and  
111 Lamothe, 2001) (transition [d] in Fig. 1), which we summarised in Sec. 5.6. Instead, Trautmann et  
112 al. (1999a) preferred a model already suggested by Schön et al. (1942) and Klasens (1946) for  
113 sulphide phosphors, with a proposed transfer of holes from the valence band to the IRSL trap  
114 throughout irradiation, effectively increasing the defects trapping capacity (transition [e] in Fig.  
115 1).

116 To address the different bleaching behaviour of IR-RF and IRSL signals, Trautmann et al. (2000a)  
117 modified their earlier model, relating the bleaching of the IRSL signal to localized electron  
118 transitions after the suggestion by Poolton et al. (1995). Following IR exposure, an electron is only  
119 excited to the excited state of the trap ([f] in Fig. 1), which is paired with the excited state of a  
120 neighbouring recombination centre, allowing a localized transition. Thus, the IRSL emission  
121 would relate to the radiative relaxation of the electron to the ground state of the recombination  
122 centre. Trautmann (2000) and Trautmann et al. (2000a) determined from pulse-annealing  
123 experiments that bleaching of the IRSL trap is limited by the number of available recombination  
124 centres, suggesting thermal instability of trapped electrons could reduce the density of holes. They  
125 drew this conclusion from the IR-RF signal's stability up to temperatures of 400 °C, whereas IRSL  
126 and the related VIS-RF signals depleted at temperatures >300 °C. Trautmann (2000) and  
127 Trautmann et al. (2000a) concluded that the IRSL electron-hole population accounts for only ~1.5

128 % of the total potential IRSL trap occupancy, implying that most of these trapped electrons do not  
129 have the possibility of recombining with a hole during IR stimulation. A phenomenon that  
130 Trautmann (2000) and Trautmann et al. (2000a) did not consider, and which may influence these  
131 effects to some extent, is athermal signal loss (i.e., anomalous fading). Following the model of  
132 Huntley (2006), ground state tunnelling [d in Fig. 1] would result in preferential recombination of  
133 unstable charge with proximal recombination centres, which may otherwise have been involved in  
134 localized transitions from the IRSL trap. Athermal de-trapping results in a non-linear increase of  
135 IRSL with dose, an effect recorded and highlighted by Trautmann (2000) and Trautmann et al.  
136 (2000a).

## 137 **2.1 Defects related to IR-RF and IRSL**

138 The exact identification of defects responsible for electron and hole trapping in feldspar is subject  
139 to ongoing research, and as such, the physical nature of the IRSL and IR-RF trap remains under  
140 debate. The traps and recombination centres of K-feldspars have mainly been assigned based on  
141 indirect measurements and correlation studies (e.g., Baril and Huntley, 2003a; Erfurt 2003a, b;  
142 Erfurt and Krbetschek, 2003b). Krbetschek et al. (1997) discussed the principal K-feldspar  
143 luminescence emissions and their possible origins for different excitation methods. The most  
144 common emission bands for K-feldspar are listed in Table 1 (please also note the references given  
145 therein).

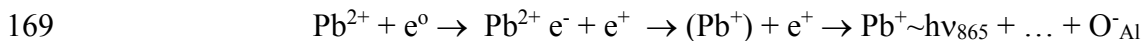
146 *Table 1*

### 147 *(Traps and recombination centres)*

148 It appears that in the literature  $\text{Fe}^{3+}$  and  $\text{Pb}^{2+}$  ions have been identified as the main centres which  
149 are believed to be responsible for the presence of the red to deep-red emission ( $\sim 1.7$  eV; Prasad  
150 and Jain, 2018) in feldspar. Kumar et al. (2018) tried to correlate their IR-PL findings (Prasad et  
151 al., 2017) with the IR-RF signal. Their work suggested that the same defect participated in the  
152 production of IR-RF and IR-PL. However, they speculated that IR-PL, contrary to IR-RF, is “site-  
153 selective”, i.e. IR-PL preferentially probes centres leading to the emission at ca 1.30 eV (955 nm)  
154 whereas the IR-RF emission may be ‘contaminated’ by emissions from other centres, such as  $\text{Fe}^{3+}$ ,  
155 related to the emission band near 680 nm to 740 nm (e.g., Geake et al., 1977; Telfer and Walker,  
156 1975; White et al., 1986; Brooks et al., 2002; Finch and Klein, 1999; Krbetschek et al., 2002;

157 Prasad and Jain, 2018). Most recent work by Kumar et al. (2020), reporting infrared  
158 cathodoluminescence (IRCL) experiments at 7 K, give evidence for a correlation of emission peak  
159 position and K-concentration. They further propose  $\text{Fe}^{4+}$  as a defect competing for electrons with  
160 the principal trap. Furthermore, the red emission's peak location has been observed to be related to  
161 the composition of feldspar samples (e.g., Finch and Klein, 1999; Krbetschek et al., 2002). In  
162 contrast, the  $\text{Pb}^+$  centre appears to be related to the IR-RF emission bands between ca. 860 nm and  
163 910 nm (e.g., Nagli and Dyachenko, 1988; Erfurt 2003a, b; Erfurt and Krbetschek, 2003a).

164 Erfurt (2003a) and Erfurt and Krbetschek (2003a) observed an increase of IR-RF signal intensity  
165 with increasing Pb content for concentrations on the order of 30 ppm to 1,400 ppm, and proposed  
166 that the IR-RF emission may be associated with the excitation of  $\text{Pb}^{2+}$  to monovalent  $(\text{Pb}^+)^*$  which  
167 subsequently relaxes to the ground state of  $\text{Pb}^+$ , emitting photons at 1.43 eV. Schematically it reads  
168 (adapted from Ostrooumov 2016, p. 152 for amazonite):



170 However, this hypothesis remains unproven, and earlier electron paramagnetic resonance (EPR)  
171 studies have indicated that  $\text{Pb}^+$  is only found in amazonite, a specific type of microcline where  $\text{Pb}^+$   
172 occupies a  $\text{K}^+$  position (Marfunin and Bershov, 1970; Marfunin, 1979). In contrast, Poolton et al.  
173 (2002b) hypothesised that the IRSL trap is a simple hydrogenic defect, calculating an optical  
174 transition at  $1.48 \pm 0.04$  eV, close to that observed in the K-Na feldspar series.

## 175 **2.2 IR-RF model and related phenomena**

176 Since Trautmann et al. (1998, 1999a, 2000a) proposed a model to explain the processes of (IR)-  
177 RF of feldspar, our understanding of luminescence processes in feldspar has improved  
178 considerably, driven mainly by the developments around conventional IRSL (e.g., Wallinga et al.,  
179 2000; Huntley and Lamothe, 2001; Lamothe et al., 2003; Auclair et al., 2003; Murray et al., 2009;  
180 Kars and Wallinga 2009; Pagonis and Kulp, 2017; Pagonis et al., 2013, 2019; Lamothe et al.,  
181 2020), the post-IR IRSL (also pIRIR) measurement protocols (Thomsen et al., 2008; Buylaert et  
182 al., 2009), time-resolved IRSL investigations (e.g., Jain and Ankjær, 2011) as well as IR-PL  
183 (Prasad, 2017; Prasad et al., 2017, 2018; Kumar et al., 2020).



184 Figure 1 shows a band-gap diagram which describes models for IRSL, post-IR IRSL and IR-RF.  
185 The presence and importance of the sub-conduction band tail-states are now widely recognized  
186 (Poolton et al., 2002a, 2009; Jain and Ankjærgaard, 2011) and anomalous fading (athermal signal  
187 loss; Wintle, 1973 for TL; Spooner 1992 for stimulation at 514.5 nm and ~880 nm) from the IRSL  
188 trap is generally regarded as ubiquitous in feldspar (e.g., Huntley and Lamothe, 2001) (transition  
189 [d] in Fig. 1). The largest inconsistency between the IR-RF models and more recent studies is that  
190 the former models did not consider the effects of hole distribution (i.e., recombination distance)  
191 and anomalous fading.

192 Excitation spectra of feldspar revealed the characteristic resonance at ~1.4 eV (1.43 eV, Hütt et  
193 al., 1988; see also above), which is superimposed on a rising continuum, now recognized as  
194 relating to the sub-conduction band-tail states (Poolton et al., 2002a, 2009). IRSL preferentially  
195 samples electrons which can recombine with proximal holes, either through tunnelling from the  
196 ground state of the IRSL trap (transition [d] in Fig. 1) or via a localized transition (transition [f] in  
197 Fig. 1). Higher energy stimulation of the IRSL trap or higher temperature stimulation (phonon-  
198 assisted diffusion) allows electrons to recombine via diffusion through the band-tail states (Poolton  
199 et al. 2002a; Jain and Ankjærgaard, 2011) (transition [g] in Fig. 1). For post-IR IRSL signals,  
200 which are measured at elevated temperatures of typically 225 °C or 290 °C (pIRIR<sub>225</sub> or pIRIR<sub>290</sub>),  
201 this enables more distal recombination centres to be accessed (Jain and Ankjærgaard, 2011), which  
202 have greater athermal (Huntley 2006; Jain and Ankjærgaard, 2011) and thermal stability (Thomsen  
203 et al., 2010; Li and Li, 2011b, 2013; Fu et al., 2012). However, pIRIR signals are systematically  
204 harder to bleach than IRSL signals (e.g., Li and Li, 2011a).

205 In general, the IR-RF signal is known to bleach less efficiently than the low-temperature IRSL  
206 signal with infra-red light (Trautmann, 1999; Trautmann et al., 1999a; Frouin, 2014; Frouin et al.,  
207 2015) and recently it has been shown that the bleaching rate is similar to that observed for the  
208 pIRIR<sub>290</sub> signal (Frouin et al., 2017). This comparably slow bleachability agrees with the  
209 apparently high thermal stability of the IR-RF signal (at least up to 350 °C, cf. preheat vs curve  
210 shape experiments by Erfurt and Krbetschek, 2003b, their Fig. 7). However, further investigations  
211 are required to constrain the thermal stability of IR-RF signal and its susceptibility to anomalous  
212 fading.

### 213 **3 Measurement devices**

214 The first IR-RF studies were carried out on home-made systems (Trautmann et al., 1998, 1999a;  
215 Schilles and Habermann, 2000; Erfurt et al., 2003), which differ from the ready-to-use systems  
216 available today (Lapp et al., 2012; Richter et al., 2013). The device described in Trautmann et al.  
217 (1998) was equipped with a spectrometer for K-feldspar IR-RF exploration. However, because the  
218 spectrometer was limited to 800 nm (Trautmann et al., 1998, 1999b), first peak investigations were  
219 based on signal extrapolation (Trautmann et al., 1998). After identifying the dose-dependent peak  
220 (Trautmann et al., 1999a) at 865 nm, the integrated RF signal around this peak was used for RF  
221 dose estimation. Schilles and Habermann (2000) and Erfurt (2003b) went one step further and  
222 attached a photomultiplier tube with a filter combination optimized to limit the measured  
223 luminescence to the 865 nm emission closely. Tables 3 and 4 summarize the details of various  
224 instruments concerning signal detection and sample bleaching parameters. Figures 2 A–D provide  
225 different technical realizations for measuring the RF signal from K-feldspar samples.

226 *Figure 2 A B C D*

227 *(All IR-RF devices)*

#### 228 **3.1 Stimulation or irradiation unit**

229 Radiofluorescence (RF) is the light emission caused by ionizing radiation. Therefore, stimulation  
230 sources can either be ionizing charged particles (ions, electrons or protons) or high energy photons  
231 (X-ray or  $\gamma$ -ray). The custom-made devices were equipped with  $^{137}\text{Cs}/^{137}\text{Ba}$  sources ( $t_{1/2} \sim 30.08$  a)  
232 (Schilles and Habermann, 2000), while other (commercially) available RF equipment has  $^{90}\text{Sr}/^{90}\text{Y}$   
233 sources ( $t_{1/2} \sim 28.8$  a) (Lapp et al., 2012; Richter et al., 2012, 2013). Details of the radiation sources  
234 are provided in Table 2. The major differences between these radiation sources are activity,  
235 radiation type and energy spectra. The  $^{137}\text{Cs}/^{137}\text{Ba}$  radiation sources in the home-made devices,  
236 e.g., used by Trautmann et al. (1999a), Schilles (2002) and Erfurt et al. (2003), emit  $\beta$ -particles  
237 and  $\gamma$ -photons with mean energies of 187.1 keV and 662 keV, respectively. At the same time,  $^{137}\text{Cs}$   
238 is also a  $\gamma$ -photon emitter, but the IR-RF stimulation by  $\gamma$ -rays was considered being negligible in  
239 comparison to the  $\beta$ -particles (Trautmann, 1999, p. 16). The  $^{90}\text{Sr}/^{90}\text{Y}$  source emits a broad energy  
240 spectrum with mean  $\beta$ -energies around 195.8 keV. Other differences regarding the stimulation

241 sources are the design and the way of irradiating the sample (planar radiation source geometry vs  
242 ring source geometry). The ring source design (Richter et al., 2012) allows the detector to be  
243 mounted directly above the source. For the planar sources, the light collection is realized by an  
244 optical light guide (Lapp et al., 2012) or using light reflected to the detector (Schilles, 2002). The  
245 indirect light collection has the advantage of reducing unwanted signal contributions induced in  
246 the detection system due to bremsstrahlung, but it usually comes at the cost of reduced detection  
247 efficiency. Additionally, the ring-type sources have been reported as delivering a highly spatially  
248 homogenous dose rate (Richter et al., 2012), relative to planar sources. Common to all types of  
249 sources and geometries is the underlying assumption of measuring a comparable IR-RF signal.

250 ***Table 2***

251 ***(Irradiation units)***

252 **3.2 Detection and filter combination**

253 Initial studies on IR-RF were based on spectrometer measurements to identify IR-RF peaks and  
254 characterize their behaviour. Trautmann et al. (1998) identified the presence and behaviour of the  
255 IR-RF peak around 854 nm based on curve fitting of a partially measured peak, but later  
256 (Trautmann et al., 1999a, b) reassigned the peak position to 865 nm using an improved  
257 spectrometer. Erfurt (2003b) and Schilles (2002) studied this peak in detail with a spectrometer  
258 and a photomultiplier tube in conjunction with optical filters (Sec. 5.1). The spectrometers' relevant  
259 details are provided in Table 3, and Fig. 3 shows the efficiency of different spectrometer systems.

260 ***Table 3***

261 ***(Spectrometer overview)***

262 ***Figure 3***

263 ***(Spectrometer transmission)***

264 Table 4 provides detailed detector settings applied to measure the IR-RF signal. The main  
265 difference between the devices is the filter combination, and thus the detection window. However,  
266 all types of filters centre around 865 nm and the usage of different filters reflects mainly the  
267 availability of filters when the equipment was delivered. Trautmann et al. (1999a) recommended  
268 centring around 865 nm and avoiding interference from the 710 nm peak. This idea was also

269 followed by Erfurt and Krbetschek (2003b) using a detection window of  $865 \pm 20$  nm, considering  
270 the broadening effect of the 710 nm peak with increasing dose (Sec. 5.1). The devices used by  
271 Schilles (2002) and Erfurt (2003b) both had the same type of photomultiplier tube (PMT)  
272 (Hamamatsu R943-02) with a quantum efficiency of  $\sim 5$  % at 865 nm. The quantum efficiency of  
273 commercial *lexsyg* and *Risø* readers is about  $\sim 12$  % at that wavelength, both employing the same  
274 PMT (Hamamatsu H7421-50), but the efficiency drops to 0.001 % for wavelengths  $> 900$  nm. The  
275 PMTs of these commercial devices have a lower efficiency for the potentially interfering signals  
276  $> 900$  nm but relatively high efficiency for the 710 nm peak (Erfurt and Krbetschek, 2003b), which  
277 might significantly interfere with the main IR-RF peak. The bandpass for different systems used  
278 in the past and present are shown in Figs. 4 A and B.

279 **Table 4**

280 *(detector settings)*

281 **Figure 4 A B**

282 *(PMT efficiency and filter combinations)*

283 **3.3 Bleaching units**

284 Table 5 summarizes the information on the commonly used bleaching units. In the device used by  
285 past researchers (e.g., Schilles and Habermann, 2000; Erfurt et al., 2003) the sample geometry was  
286 fixed, i.e., the sample was not moved between different measurement steps. Thus, the IR-RF  
287 signal's bleaching was done by connecting a solar lamp using an optical fibre. In this design, IR  
288 cut-off filters were used to avoid excess heating due to the high intensity of light of the solar lamp.  
289 In contrast, inside commercial devices for IR-RF measurement and bleaching (e.g., *lexsyg* and  
290 *Risø*) the sample moves to different positions. The *Risø* system is equipped with powerful UV  
291 LEDs ( $\sim 700$  mW), and the *lexsyg* device has an inbuilt LED solar simulator that combines up to  
292 six wavelengths with the option of varying the power of each LED (Richter et al., 2013; see Table  
293 5).

294 **Table 5**

295 *(bleaching units)*

### 296 **3.4 Sample geometry**

297 Krbetschek et al. (2000) and Erfurt and Krbetschek (2003b) recommended a fixed geometry during  
298 IR-RF measurements. They observed a high dispersion in IR-RF dose distributions attributed to  
299 geometry changes (e.g., grain movements) when samples were bleached outside the reader.  
300 Buylaert et al. (2012) did not observe any changes in the IR-RF signal due to the movement of the  
301 sample from one position to another (cf. Fig 3b in Buylaert et al., 2012). Similarly, Frouin et al.  
302 (2015, 2017) did not report dose dispersions caused by the movement of the sample inside the  
303 reader for their measurements using a *lexsyg research* reader. Later, Kreutzer et al. (2017)  
304 attributed a large part of the inter-aliquot scatter to unwanted machine-induced geometry changes,  
305 which, however, may have affected only their particular reader. Nevertheless, in summary, it  
306 appears to be advisable to aim for a stable sample geometry and check the results for unwanted  
307 effects, enlarging the  $D_e$  distribution (cf. Kreutzer et al., 2017).

### 308 **4 Sample preparation methods**

309 IR-RF sample preparation methods extract K-feldspar enriched mineral grains following routine  
310 procedures (e.g., Preusser et al., 2008). After sieving and chemical treatments with HCl and H<sub>2</sub>O<sub>2</sub>,  
311 density separation using heavy-liquids (e.g., lithium heteropolytungstates or sodium polytungstate)  
312 extract feldspar grains. Additional (froth) flotation (e.g., Herber 1969; application examples:  
313 Miallier et al., 1983; Sulaymonova et al., 2018) can be applied to enrich the K-feldspar  
314 concentration further; a procedure that the Freiberg group has mainly used in the context of IR-RF  
315 (e.g., Trautmann, 1999; Erfurt 2003b). Flotation likely provides a better yield in terms of better  
316 separation of quartz and feldspar mineral phases. Despite requiring extra laboratory equipment and  
317 staff training, flotation has unmined potential for further enriching the K-feldspar fraction (e.g.,  
318 via selective flotation: Larsen et al., 2019) with possible implications for measured IR-RF signals.

319 To remove the outer  $\alpha$ -irradiation affected layer of coarse K-feldspar grains ( $> 90 \mu\text{m}$ ) a low  
320 concentration ( $\leq 10\%$ ) HF treatment was often used (e.g., Wagner et al., 2010; Lauer et al., 2011).  
321 However, the practice of etching of coarse grain K-feldspar was already questioned by Duller  
322 (1992), who described non-uniform etching along the lines of weakness within the mineral. Porat  
323 et al. (2015) recalled caution if HF is applied to feldspar grains because HF etching might  
324 significantly modify the luminescence properties of K-feldspar, and thus Porat et al. (2015) suggest

325 etching times <15 min. Frouin et al. (2017) reported inconclusive, younger and highly scattered,  
326 IR-RF results for two samples (BT714, BT715) after prolonged HF treatment (10 %, 40 min),  
327 while this was not observed for another, non-etched, sample from the same site (BT706). Although  
328 the systematic effect of HF treatments with different timings and concentration on the IR-RF signal  
329 remains unexplored, HF treatment appears to be dispensable.

## 330 **5 IR-RF signal characteristics**

### 331 **5.1 IR-RF spectroscopy: Signal identification and measurement optimization**

332 The IR-RF signal composition was extensively studied using a home-made spectrometer in  
333 combination with a liquid nitrogen-cooled charged coupled device (CCD) detector (Trautmann et  
334 al., 1998, 2000b; Krbetschek and Trautmann, 2000). Their spectroscopic investigations of IR-RF  
335 from feldspar revealed many peaks centred at various wavelengths. However, the 865 nm emission  
336 peak was found to be stable with its intensity decreasing with increasing dose. K- feldspar showed  
337 the highest signal intensity at this wavelength compared to other feldspar compositions. Trautmann  
338 (1999) and Schilles (2002) noticed that the spectrum of K-feldspar could be fitted with two  
339 Gaussian functions centred at 710 nm (1.75 eV) and 865 nm (1.43 eV). Later, Erfurt (2003b)  
340 improved the spectrometer used by Trautmann (1999) and recognized that the data required a  
341 minimum of three Gaussian functions to fit the emission spectrum, with a third emission centred  
342 at ~910 nm (1.35 eV; Erfurt and Krbetschek, 2003a). The spectroscopic study of these peaks  
343 provided the appropriate detection range (filter combination) required for isolating the main IR-  
344 RF peak at 865 nm from other neighbouring emissions (Krbetschek et al., 2000). A typical raw  
345 spectrum for K-feldspar shows many emission peaks (Fig. 5C after Schilles, 2002) and Trautmann  
346 et al. (1999a) demonstrated that the peak intensity at 865 nm decreases with increasing dose,  
347 whereas the intensity of the 710 nm peak increases with dose. Furthermore, Trautmann et al. (1998)  
348 observed that the 710 nm peak is unstable and vanished within a few hours following irradiation.  
349 Both the 710 nm and 910 nm<sup>1</sup> emissions may interfere with the main IR-RF peak (865 nm), which  
350 filters can minimise. The effect of such a filter can be simulated using three superimposed Gaussian

---

<sup>1</sup>920 nm in Erfurt and Krbetschek (2003b), however, henceforth termed '910 nm' emission.

351 functions (Fig. 5A and Fig. 5B similar to Erfurt and Krbetschek, 2003b). Table 4 summarizes all  
352 devices' filter combinations to isolate the peak centred at a wavelength of 865 nm.

353 ***Figure 5 A B C***

354 ***(IR-RF peaks in feldspar)***

355 **5.2 IR-RF signal resetting**

356 The success of (optical) luminescence dating methods relies on resetting the luminescence signal  
357 during sediment transport prior to burial. For IR-RF, the signal intensity increases with light  
358 exposure after several minutes to several hours and reaches its highest value when all traps are  
359 empty. The bleachability of the IR-RF signal was assessed by bleaching until a plateau is formed  
360 between the IR-RF signal vs bleaching time. A constant plateau indicates no further signal  
361 increase, i.e., the IR-RF signal is at its maximum, and all IR-RF related traps are empty. In the first  
362 IR-RF bleaching experiments (Trautmann et al., 1999a), natural direct sunlight (VIS to UV  
363 component, Fig. 6A) was used for a few hours (between 2 h and 5 h of daylight exposure in  
364 February in Freiberg, Germany) to bleach the IR-RF signal. Later, Trautmann et al. (2000a)  
365 showed that wavelengths shorter than 500 nm were more efficient at resetting the IR-RF signal  
366 (Fig. 6B) and Krbetschek et al. (2000) demonstrated that only a few minutes (~5–10 min) were  
367 required to reset the signal, using a 200 W Hg-lamp (Table 5 for an overview of the settings) along  
368 with a heat-absorbing filter (Fig. 6C). Further bleaching experiments were conducted using a 300  
369 W OSRAM ‘Ultravitalux’ sunlamp placed at a distance of 35 cm from the aliquot for 6.5 h  
370 (Krbetschek et al., 2000) or an on-board lamp (250 W OSRAM metal halide), using fibre optics,  
371 which delivered ~100 mW cm<sup>-2</sup> to the aliquot for 30 min.

372 ***Figure 6 A B C D***

373 ***(Bleaching)***

374 Buylaert et al. (2012) compared the D<sub>e</sub> values of samples with independent age control. They  
375 obtained different values between aliquots that were bleached with UV LEDs (delivering 700  
376 mW cm<sup>-2</sup>) with an exposure time of 25 min, compared to bleaching with a Hönle SOL 2 solar  
377 simulator for 4 h. Samples bleached with the Hönle SOL2 resulted in older, but partly also more  
378 consistent ages compared to the independent age control (cf. Buylaert et al., 2012, their Fig. 7).

379 Later Varma et al. (2013) concluded that exposure of 800 s is optimal for resetting the IR-RF signal  
380 using the aforementioned UV LED (delivering  $700 \text{ mW cm}^{-2}$ ).

381 Frouin et al. (2015) systematically compared the bleaching behaviour of monochromatic light and  
382 a solar simulator spectrum. In their study, they showed that: i) K-feldspars of various origins  
383 exhibit the same behaviour during bleaching experiments, and ii) the IR-RF signal can be bleached  
384 by all wavelengths, ranging from 365 nm to 850 nm, and iii) the IR-RF signal can be completely  
385 reset in nature and cannot be “over-bleached” in the laboratory even with the use of longer time  
386 exposures. Finally, they recommend a solar spectrum close to the terrestrial solar spectrum with  
387 minimal UV light contribution. They achieved this by individually adjusting the monochromatic  
388 LEDs' power in their luminescence reader and stated that this spectrum delivered a sufficient  
389 amount of power ( $375 \text{ mW cm}^{-2}$ ) to bleach the IR-RF signal in minimum time at ambient  
390 temperature (Frouin et al., 2015). Furthermore, they showed that the onset of a bleaching plateau  
391 started after 3 h to 4 h of light exposure (cf. Fig. 4 in Frouin et al., 2015). Specifically, within this  
392 light spectrum, the power of the UV (325 nm) LED was reduced to  $10 \text{ mW cm}^{-2}$  as this wavelength  
393 is absorbed by the atmosphere and its presence in the terrestrial solar spectrum is minimal.  
394 Regardless, this low power, Frouin (2014, her Fig. 28) showed that UV bleaches most efficiently  
395 within the first seconds before it reaches a plateau after ca. 40 h. Although an artificial bleaching  
396 spectrum using only six wavelengths (LEDs) cannot match the terrestrial solar spectrum, it may  
397 remain a good approximation of natural bleaching conditions (typical irradiance on Earth of 90–  
398  $100 \text{ mW cm}^{-2}$ ; ASTM international, 2012). A comparison between the bleaching behaviour of the  
399 IR-RF signal measured at  $70 \text{ }^\circ\text{C}$  (Sec. 6.1) with other variants of the IRSL signals of K-feldspar  
400 showed that IR-RF seems to bleach at a similar rate to the pIRIR<sub>290</sub> signal but much slower than  
401 the IRSL<sub>50</sub> signal (Frouin et al., 2017; Fig. 6D). However, a similar bleaching rate compared to the  
402 pIRIR<sub>290</sub> signal does not guarantee a complete reset of either signal (i.e., pIRIR<sub>290</sub> and IR-RF);  
403 various studies have shown that the pIRIR<sub>290</sub> signal is hard to bleach and can have large residual  
404 doses even after 4 h of solar simulator bleaching (e.g., Buylaert et al., 2012; Li et al., 2014). It may  
405 take up to ~300 h to reach a constant residual dose (Yi et al., 2016). In summary, Frouin et al.  
406 (2015) recommended a minimum of 3 h bleaching using the inbuilt solar simulator of their  
407 equipment with the following settings: 365 nm ( $10 \text{ mW cm}^{-2}$ ), 462 nm ( $63 \text{ mW cm}^{-2}$ ), 525 nm ( $54$   
408  $\text{mW cm}^{-2}$ ), 590 nm ( $37 \text{ mW cm}^{-2}$ ), 623 nm ( $115 \text{ mW cm}^{-2}$ ), and 850 nm ( $96 \text{ mW cm}^{-2}$ ).



### 409 5.3 Phosphorescence

410 In the context of IR-RF, two types of phosphorescence have been observed: (1) Phosphorescence  
411 after bleaching (Fig. 7) and (2) phosphorescence after irradiation (so-called  
412 radiophosphorescence). *Phosphorescence after bleaching* was considered by Erfurt and  
413 Krbetschek (2003b). They recognized that K-feldspar samples, bleached with a solar simulator,  
414 show a very strong phosphorescence at 865 nm. For a sediment sample with a palaeodose of  
415 ~1,500 Gy, extrapolation of the phosphorescence signal at room temperature using an exponential  
416 decay shows that its effect lasts beyond 1,000 s after bleaching (cf. Fig. 6 in Erfurt and Krbetschek,  
417 2003b). To accommodate this effect in IR-RF measurement protocols, Erfurt and Krbetschek  
418 (2003b) recommended a pause of one hour after bleaching, before starting the next IR-RF  
419 measurement. In contrast, Buylaert et al. (2012) showed that after bleaching the phosphorescence  
420 signal intensity is lower by two orders of magnitude than IR-RF, its effect on the main IR-RF  
421 signal will be negligible. However, it should be noted that their setup differs from the one used by  
422 Erfurt and Krbetschek (2003b) (Sec. 3). Varma et al. (2013) reported that although the IR-RF  
423 signal of their sample was almost at its saturation level, it did not show significant phosphorescence  
424 after bleaching the sample for 800 s. Hence, they concluded that no extra pause is needed and  
425 suggested that a delay of 500 s is sufficient to reduce the phosphorescence down to the background  
426 level if the bleaching time is less than 800 s. Similarly, Schaarschmidt et al. (2019) reported a weak  
427 phosphorescence compared to the IR-RF signal and reduced the pause to 900 s for their samples.  
428 In summary, it seems that phosphorescence caused by bleaching can be avoided by introducing a  
429 pause of 15 min to 1 h prior to IR-RF measurements (Erfurt and Krbetschek, 2003b; Frouin et al.,  
430 2015; Schaarschmidt et al., 2019) in the case of solar simulator bleaching and may not be required  
431 if the sample is bleached with a UV LED for 800 s or longer (Varma et al., 2013).

432 *Radiophosphorescence* is a known phenomenon used in the past to characterize luminescence  
433 spectra from feldspar (e.g., Krbetschek and Rieser, 1995; Baril and Huntley, 2003b). Varma et al.  
434 (2013) observed phosphorescence with an intensity of ~35 % of the IR-RF signal (cf. Fig 2b in  
435 Varma et al., 2013) immediately after irradiation up to 800 Gy. Phosphorescence caused by  
436 irradiation can be a severe issue since IR-RF measurements need continuous irradiation during  
437 signal measurement. Thus, phosphorescence superposition onto the main IR-RF signal can be  
438 problematic and might be as high as 35 % of the IR-RF signal (Varma et al., 2013). Nevertheless,

439 if the phosphorescence intensity is independent of the previously administered radiation dose, it  
440 might be neglected. In contrast, if the radiophosphorescence is dose-dependent, it will be  
441 impossible to isolate it from the IR-RF signal. This possible superposition of IR-RF and  
442 radiophosphorescence needs to be further investigated.

443 *Figure 7*

444 *(Phosphorescence)*

445 **5.4 IR-RF sensitivity**

446 Schilles and Habermann (2000) conducted a bleaching study on natural and commercially  
447 available K-feldspar samples. Two repeated cycles of 20 h of sunlight bleaching resulted in  
448 different IR-RF intensities and changes in the shape of the decay curve for each bleaching cycle.  
449 Natural and commercial samples showed different bleaching levels and a relative change of signal  
450 intensity of 3.6–4.8 % for natural sunlight and 5.1–8.9 % for artificial solar simulation (SOL2,  
451 Hönle). These variations in signal intensity indicated sensitivity changes due to bleaching and/or  
452 irradiation during the measurement. In order to cope with this, Schilles (2002) suggested using a  
453 separate aliquot and measuring its IR-RF for two bleaching cycles. Based on these additional  
454 measurements, a dimensionless correction factor could be derived from the ratio of the regenerated  
455 IR-RF intensities (Fig. 8A).

456 Similarly, Varma et al. (2013) reported sensitivity changes during measurement and could not  
457 recover a given dose using IR-RF. They derived a sensitivity correction factor  $F_S$  by repeating the  
458 bleaching and regenerative IR-RF six times.  $F_S$  (also Sec. 6.1) is estimated from the ratio of IR-RF  
459 intensity of the first regenerated cycle to the extrapolated intensity of the zeroth cycle (Fig. 8B).  
460 Furthermore, Varma et al. (2013) recognized that all six sediment samples investigated in their  
461 study needed a sensitivity correction to obtain reasonable dose recovery results. Erfurt and  
462 Krbetschek (2003b) also showed a shape mismatch and change in intensity for multiple  
463 measurements but demonstrated that this sensitivity change would only affect the dose estimation  
464 by 3 % (cf. Fig 4 in Erfurt and Krbetschek, 2003b). In addition to these studies, Buylaert et al.  
465 (2012) mentioned the possibility of a significant sensitivity change, either induced by bleaching or  
466 by the IR-RF measurement itself.

467 Frouin et al. (2017) reported on a curve shape mismatch between the natural IR-RF ( $RF_{\text{nat}}$ ) and the  
468 regenerated IR-RF ( $RF_{\text{reg}}$ ) curve (cf. Fig. 2 in Frouin et al., 2017), and rejected the measured  
469 aliquots (Fig. 8C). In the literature, two attempts have been made to explain this behaviour:  
470 Kreutzer et al. (2017) gave evidence that a technical artefact with the measurement equipment  
471 caused an unwanted geometry change. Murari et al. (2018) investigated the possible reason for this  
472 shape mismatch using three modern bleached samples in a dose recovery study. For these samples,  
473 a given dose was recovered using the  $RF_{\text{nat}}$  and  $RF_{\text{reg}}$  signals. In their study,  $RF_{\text{nat}}$  refers to IR-RF  
474 curves from the naturally bleached modern sample, and  $RF_{\text{reg}}$  refers to IR-RF curves measured  
475 after bleaching with the solar simulator. As samples are bleached in both cases, both IR-RF curves,  
476  $RF_{\text{nat}}$  and  $RF_{\text{reg}}$ , can act as regenerated IR-RF curves. An offset of 23 % was observed when the  
477 dose was recovered from the  $RF_{\text{nat}}$  signal (cf. Fig. 2 in Murari et al., 2018) while all the samples  
478 were able to recover the known dose from the  $RF_{\text{reg}}$  signal with an uncertainty of 4 %. Their  
479 findings showed the discrepancy in dose recovery and the mismatch of the shape of  $RF_{\text{reg}}$  curves  
480 compared to  $RF_{\text{nat}}$  curves. The latter is attributed to the change in IR-RF sensitivity. Possible causes  
481 for these sensitivity changes are the high photon flux of the built-in solar simulator, the high  
482 laboratory dose rate and/or the interference from other neighbouring peaks with the main IR-RF  
483 signal (i.e., 710 nm and 910 nm emissions; Trautmann, 1999; Erfurt and Krbetschek, 2003b). In  
484 summary, it seems that IR-RF is affected by sensitivity changes that should be monitored and  
485 corrected. Based on their findings, Murari et al. (2018) suggested a new analysis and correction  
486 method named the ‘*horizontal and vertical correction*’ method (Sec. 6.2).

### 487 *Figure 8*

#### 488 *(Sensitivity change monitoring)*

## 489 **5.5 IR-RF initial rise**

490 A few IR-RF studies mentioned an unexpected signal rise at the beginning of the IR-RF  
491 measurement (e.g., Schilles, 2002; Buylaert et al., 2012; Frouin, 2014; Huot et al., 2015; Frouin et  
492 al., 2017). It was often described as a bump, a TL-like peak or an initial rise of the RF signal (Fig.  
493 9A; for further discussions on the dynamic range see below) and it typically persisted for the first  
494 few hundred seconds (~6–12 Gy) before the IR-RF starts decaying monotonically (Huot et al.,  
495 2015). According to Frouin et al. (2017), the initial rise in the natural signal seemed to be positively

496 correlated with the equivalent dose ( $D_e$ ) (cf. Fig. S7 in Frouin et al., 2017) of a sample and was  
497 observed for every K-feldspar sample used in their study.

498 In contrast, the Freiberg group never reported such IR-RF behaviour (e.g., Krbetschek et al., 2000;  
499 Erfurt, 2003b) leading to speculation that differences in instrumental design (overall system  
500 efficiency, different detection bandpass filter combinations or radiation source strengths) may  
501 cause the effect or favour its detection. Measurements using both commercial devices (*lexsyg*  
502 *research* and *Risø*, Sec. **Error! Reference source not found.**) showed the initial rise behaviour  
503 (e.g., Huot et al., 2015; Frouin et al., 2017; Qin et al. 2018). However, this is not discussed in detail  
504 by Buylaert et al. (2012) who discarded the signal corresponding to the first ~20 Gy from their  
505 data analysis considering it as a sample-specific behaviour.

506 Huot et al. (2015) thoroughly investigated the origin of the initial rise after bleaching (regenerated  
507 signal). They hypothesized that the rapid increase in RF observed at the beginning of the  
508 irradiation, is not due to higher electron trapping, but can be explained by thermally assisted  
509 phosphorescence. “Minute variations in sample temperature” (Huot et al., 2015, p. 241) can cause  
510 this peak because of the existence of shallow traps which emit phosphorescence in the near-  
511 infrared region. Their recommendation to avoid this peak was to wait at least 1 h after bleaching,  
512 let the sample cool down to room temperature, or measure IR-RF at elevated temperatures of  
513 around 70 °C to 100 °C. Nevertheless, the phenomenon does not seem to disappear from the IR-  
514 RF signal even when measured at elevated temperatures of 70 °C and waiting for one h after  
515 bleaching (cf. Fig. 2 vs Fig. 7 in Frouin et al., 2017).

516 Furthermore, the reported a correlation between the intensity of the initial rise in the natural signal  
517 and the sample's  $D_e$  (cf. Frouin et al., 2017 their Fig. S7), indicated that shallow TL traps alone  
518 cannot explain this phenomenon. Nevertheless, from the perspective of dating, it seems that the  
519 effect of the initial rise does not affect dose estimation as it appears only for 100 s to 200 s  
520 (typically ~6–12 Gy) in every IR-RF signal (i.e., natural and regenerated IR-RF signals). However,  
521 further investigations combined with modelling are needed to better understand the origin of the  
522 IR-RF signal increase during the first seconds.

### 523 *Figure 9*

524 *(Initial rise and dynamic range)*

## 525 **5.6 IR-RF signal stability**

526 The IR-RF signal stability has two dimensions: thermal stability and athermal stability. The first  
527 is directly related to the depth of the trap and represents the stability of the electrons captured by  
528 the defect over time, dependent on the ‘burial’ temperature. The second, also known as ‘anomalous  
529 fading’ (Wintle 1973), is temperature independent.

530 The thermal stability of the IR-RF signal was investigated by Trautmann et al. (1999a) who used  
531 pulse annealing experiments, and they reported thermal stability of the IR-RF signal up to 450 °C  
532 (Fig. 10A). However, this result was observed only for one sample (Ook1), which is >1 Ma old;  
533 two younger samples showed a decrease in signal intensity after 250 °C (Fig. 10A). Later  
534 experiments by Erfurt and Krbetschek (2003b) and Frouin et al. (2017) (Fig. 10B) confirmed these  
535 findings. Further, it was noticed that for temperatures of 250 °C and higher, natural IR-RF ( $RF_{nat}$ )  
536 signal intensities decreased with pulse annealing temperature (Fig. 10B) while they increased  
537 slightly for regenerated IR-RF signals ( $RF_{reg}$ ). If annealing at high temperatures resets the IR-RF  
538 signal, the IR-RF intensity should not decrease, which is in accordance with observations on  $RF_{reg}$ ,  
539 but in contradiction to that for  $RF_{nat}$ . This contrasting feature may be explained by a change of the  
540 IR-RF sensitivity with temperature. In thermoluminescence (TL) studies on K-feldspar rapid,  
541 temperature-induced luminescence sensitivity decreases were frequently reported (Aitken,  
542 1985a, 1998). Those changes are non-repeatable in subsequent dose cycles (cf. reasoning in Frouin  
543 et al., 2017).

544 Nevertheless, while temperatures above ca. 250 °C may impact the  $D_e$ , these observations should  
545 not be used to draw general conclusions on the thermal stability of the defect responsible for the  
546 IR-RF emission. Erfurt (2003a, b) referred to works on amazonite (cf. Ostrooumov, 2016 for an  
547 overview) and argued that the  $Pb^+$  centres are stable up to ~450 °C (Speit and Lehmann 1982) or  
548 even up to 700 °C (assumption in Erfurt, 2003b: 500 °C; 700 °C in Ostrooumov, 2016). Above this  
549 temperature, the  $Pb^+$  centre disappears (a process also referred to as de-amazonitization).

550 Krbetschek et al. (2000) presented experimental results supporting the hypothesis of long-term  
551 stability of the IR-RF signal. For instance, short-term (days to months) fading tests with storage of  
552 samples for several months at room temperature showed no sign of signal increase (i.e., no  
553 emptying of traps) which seems to confirm signal stability over short periods (at room

554 temperature). Furthermore, based on the dating of sediment samples using IR-RF, e.g., Wagner et  
555 al. (2010) and Novothny et al. (2010) claimed that the IR-RF signal exhibited no indication of  
556 fading for ages in the range ca 420–700 ka (Wagner et al., 2010) and 148–250 ka (Novothny et al.,  
557 2010). Likewise, Frouin et al. (2017) and Kreutzer et al. (2018a) reported a good agreement with  
558 the independent age control of even older ages. By contrast, Buylaert et al. (2012) showed age  
559 underestimation for older samples (>100 ka) and overestimation for younger samples (< 50 ka).  
560 They speculated whether the offset could be explained by signal instability (fading), bleachability  
561 and sensitivity change during measurement. They also showed the natural IR-RF signal from an  
562 infinitely old sample was only 84 % of the saturation, suggesting the signal might fade. However,  
563 the measurement setup by Buylaert et al. (2012) did not match the suggestions by Erfurt and  
564 Krbetschek (2003b), e.g., regarding the detection window, and should be read cautiously.  
565 Recently, Kumar et al. (2021) reinterpreted the findings by Buylaert et al. (2012). They reported  
566 IR-PL age results in agreement with independent age control. These findings indicate that IR-PL  
567 does not suffer from athermal fading or signal instability. However, since Kumar et al. (2018)  
568 hypothesised a similar trap for the IR-PL and the IR-RF, they concluded that IR-RF does not suffer  
569 from signal instability. Hence, without presenting new IR-RF data, Kumar et al. (2021, p. 14)  
570 concluded: “[...] *that the under-estimation in IR-RF [meant are the results reported by Buylaert*  
571 *et al., 2012] is likely because of sensitivity changes rather than signal stability.*” Nevertheless,  
572 beyond the research summarized above, further studies should be carried out to investigate the  
573 thermal and athermal stability in the context of IR-RF as a luminescence dating method. For IR-  
574 PL, Kumar et al. (2021) suggested tests on geological samples (~ Ma), i.e. samples in apparent  
575 dose saturation, which might also provide a good test for the IR-RF signal stability in future  
576 studies.

577 ***Figure 10 A B***

578 ***(Signal stability)***

579 **5.7 IR-RF dose limits**

580 The minimum measurable dose has not yet been systematically determined with IR-RF. While  
581 Erfurt (2003b) estimated a dose of ca 40 Gy, Frouin et al. (2017) reported measurable doses of  
582  $0.5 \pm 1.0$  Gy and  $1.2 \pm 1.9$  Gy for two modern analogue samples. Current instrument configurations

583 allow signals with a few photon-counts per second to be distinguished. In available luminescence  
584 measurement systems (Sec. 3), the IR-RF signal of K-feldspar is usually of the order of a million  
585 photon counts per second with signal intensities at its maximum when the sample is bleached, i.e.,  
586 for zero dose samples. Thus, the minimum measurable dose (limit) is a function of stimulation  
587 dose-rate ( $\text{Gy s}^{-1}$ ), the measurement channel resolution ( $\text{s channel}^{-1}$ ) and the applied statistical  
588 procedure to distinguish two bright signals and determine the  $D_e$  (e.g., the sliding method causes  
589 discretization effects, Sec. 6.2). For example, a sampling rate as applied by Murari et al. (2018) of  
590  $10 \text{ s channel}^{-1}$  for a dose rate of ca.  $0.06 \text{ Gy s}^{-1}$  would theoretically correspond to a minimum  
591 distinguishable dose of 0.6 Gy on average.

592 The IR-RF dynamic range is defined as the ratio of the maximum to the minimum of the IR-RF  
593 signal intensity. In other words, this is the ratio of the IR-RF signal from saturation to the bleaching  
594 level of the sample, which in general varies about a factor of 2 (Erfurt and Krbetschek, 2003a).  
595 The IR-RF signal dynamic range is minimal (Fig. 9B) compared to the signal dynamics from the  
596 other variants of luminescence such as OSL or IRSL, where it typically is at least an order of  
597 magnitude higher. Due to low signal dynamic ranges, the slope of IR-RF intensity ( $I$ ) with respect  
598 to dose ( $D_e$ ) changes gradually and finally approaches zero. In terms of resolving dose estimates,  
599 the resolution becomes impoverished in the higher dose region as a slight change in intensity ( $dI$ )  
600 may lead to a large uncertainty in dose estimation ( $dD_e$ ). Erfurt and Krbetschek (2003b)  
601 recommended determining the dose where the slope of signal intensity vs dose approaches a value  
602 of zero (i.e.,  $dI/dD_e \approx 0$ ). Based on this parameter, they found that for their reader configuration,  
603 IR-RF curves allow dose estimation up to  $\sim 650 \text{ Gy}$ .

604 However, the upper dose limit of IR-RF, and with it, the temporal range, is subject to ongoing  
605 research. Krbetschek et al. (2000) reported a saturation  $D_e$  value of  $1,440 \pm 215 \text{ Gy}$  (nature of the  
606 error not reported) for a single sample, and in a recent IR-RF dating study Kreutzer et al. (2018a)  
607 reported a measurable mean dose of  $1,064 \pm 41 \text{ Gy}$  (mean  $\pm$  standard deviation). Erfurt (2003b)  
608 estimated a mean saturation dose as high as 1,500 Gy. However, Erfurt (2003b) and Erfurt and  
609 Krbetschek (2003b) also estimated the maximum resolvable dose at 600 Gy to 650 Gy as the small  
610 IR-RF signal dynamic range can limit the precision of signal interpolation. The highest, single  
611 aliquot, IR-RF dose of  $4,181 \pm 371 \text{ Gy}$  (mean  $\pm$  standard deviation) was reported by Wagner et al.

612 (2010) (cf. their “Supporting Information”, Table S2) using the same instrument as Erfurt et al.  
613 (2003).

614 On a *lexsyg research* system Frouin et al. (2017) recently reported successful measurement of a  
615 ~2,100 Gy dose using a regenerated IR-RF signal that was recorded up to 4,000 Gy cumulative  
616 dose (cf. their Fig. 7 for sample TML1). Furthermore, Murari et al. (2018) demonstrated accurate  
617 laboratory dose recovery up to 3,600 Gy by interpolating onto a regenerated IR-RF curve measured  
618 up to 3,900 Gy. However, it should be pointed out that the intensity difference between 2,000 Gy  
619 and 3,500 Gy was only around 4 % (Fig. 9B for the dynamic range of IR-RF), which leaves the  
620 results susceptible to minimal intensity changes. Hence, at this moment, we cannot refer to a  
621 saturation limit of IR-RF. However, the one single value published by Murari et al. (2018) of ca.  
622 3,600 Gy would allow age determinations (dose rates in the order of 2–3 Gy ka<sup>-1</sup>) of 1.2 Ma to 1.8  
623 Ma. Whether this dose (and temporal) range is feasible for routine dating is still under debate.

## 624 **5.8 The IR-RF alpha-efficiency**

625 The ionisation efficiency and, with it, the efficiency of induced luminescence per unit dose,  
626 depends on the type of irradiation (i.e.,  $\alpha$ - vs  $\beta$ - vs  $\gamma$ -radiation). Commonly, the luminescence  
627 produced by  $\alpha$ -particles per unit dose is substantially lower than for  $\beta$ - or  $\gamma$ -radiation. Thus, the  $\alpha$ -  
628 efficiency needs to be determined to correctly calculate the  $\beta$ -equivalent  $\alpha$ -dose rate contribution  
629 (cf. Aitken, 1985a) if polymineral fine grain (4–11  $\mu\text{m}$ ) or other grain size fractions untreated with  
630 HF are used. So far, only a single study exists determining the  $\alpha$ -efficiency of K-feldspar using  
631 IR-RF. Kreutzer et al. (2018b) used an  $\alpha$ -flux calibrated <sup>241</sup>Am source. The central  $S_{\alpha}$ -value  
632 (Guérin and Valladas, 1980; Valladas and Valladas, 1982) obtained from four fine-grain K-  
633 feldspar samples (84 aliquots) was  $9.26 \pm 1.62 \mu\text{Gy}/(10^3 \alpha \text{ cm}^{-2})$ . The corresponding  
634 (dimensionless) value in the  $a$ -value system (cf. Aitken 1985b) of  $0.067 \pm 0.012$  is similar to  $a$ -  
635 values reported for IRSL polymineral fine grain (e.g., Kadereit et al., 2010). Based on these  
636 findings and if the  $\alpha$ -efficiency cannot be determined, an estimated  $a$ -value of  $0.07 \pm 0.01$  (applied  
637 to fine grain and unetched coarse grains, cf. Kreutzer et al., 2018b) appears to be justified.



638 **6 Measurement protocols and data analysis**

639 Like other luminescence measurement protocols for equivalent dose ( $D_e$ ) determination (e.g., for  
640 TL, OSL or IRSL), over the years, several measurement protocols and data analysis techniques  
641 have been proposed to determine the  $D_e$  for IR-RF.

642 **6.1 IR-RF measurement protocols**

643 The first comprehensive IR-RF measurement protocol named IRSAR (infrared single-aliquot  
644 regenerative-dose) was presented by Erfurt and Krbetschek (2003b). Frouin et al. (2017)  
645 introduced a modified version of this protocol and entitled it RF<sub>70</sub> (where the subscript '70' refers  
646 to the applied measurement temperature of 70 °C). Additionally, several other protocols have been  
647 reported in the literature and are summarized in Table 6.

648 *Table 6*

649 *(Measurement protocols)*

650 All listed protocols consist of less than six measurement steps. Common to all protocols are three  
651 main steps: (I) measurement of the natural IR-RF signal (RF<sub>nat</sub>), (II) signal resetting by bleaching  
652 and (III) measurement of the regenerated IR-RF (RF<sub>reg</sub>) signal after bleaching. The duration of the  
653 IR-RF measurements (natural, regenerative) is determined by the chosen data analysis approach  
654 (Fig. 11). For example,  $D_e$  determination via curve fitting and signal extrapolation results in IR-  
655 RF measurements of longer duration for the natural IR-RF signal than for the regenerated signal  
656 and vice versa for a  $D_e$  determination via interpolation.

657 Trautmann et al. (1999a), Krbetschek et al. (2000) and Schilles (2002) distinguished between an  
658 additive (extrapolation) and a regenerative (interpolation) measurement approach, depending on  
659 the particular IR-RF signal (natural: additive; regenerative: regenerative) used for subsequent  
660 curve fitting. However, this distinction is misleading and should be avoided as it conflicts with the  
661 commonly accepted terminology used for TL/OSL. All recorded IR-RF signal curves are dose-  
662 response curves, and signal resetting is carried out by optical bleaching. Thus, natural IR-RF  
663 curves are always additive dose-response curves, irrespective of the technique used to analyse the  
664 data and to obtain the  $D_e$ , namely: extrapolation, interpolation or sliding (see the following  
665 section).

666 *Bleaching duration:* All published protocols include an optical bleaching step to reset the natural  
667 IR-RF signal. The bleaching is either carried out by using an artificial light source or by natural  
668 sunlight. To mimic natural sunlight conditions, Frouin et al. (2015) proposed a bleaching spectrum  
669 consisting of six different wavelengths ranging from UV-A (365 nm) to NIR (850 nm), while  
670 Buylaert et al. (2012) used only a single wavelength (UV-violet LED, 395 nm) to reset the IR-RF  
671 signal. The bleaching duration is sample dependent and linked to the technical specification of the  
672 equipment, the available wavelengths, and power. Using a similar measurement setup, Varma et  
673 al. (2013) and Buylaert et al. (2012) found bleaching for 800 s and 1,500 s respectively, to be  
674 sufficient for most cases, Frouin et al. (2017) suggested solar simulator bleaching for at least  
675 10,800 s. Kreutzer et al. (2018a) suggested a bleaching test using the internal solar simulator of  
676 their *lexsyg* system. The test applied consecutive bleaching steps of 1,000 s each. A stable signal  
677 plateau indicates sufficient bleaching. Generally, it appears that longer bleaching times should be  
678 preferred to ensure the resetting of the natural IR-RF signal. For further details on the bleaching  
679 behaviour of the IR-RF signal see Sec. 5.2.

680 *Pause duration:* Five out of seven IR-RF protocols (Table 6) suggested a pause after the optical  
681 resetting of the IR-RF signal for at least 1,800 s. The pause is believed to account for an unwanted  
682 superposition of IR phosphorescence on the IR-RF signal (e.g., Erfurt and Krbetschek, 2003b).  
683 Varma et al. (2013) carried out the pause as a phosphorescence measurement just before the  
684 stimulation itself. Based on their results, it appears that the phosphorescence is induced only by  
685 the irradiation ('radiophosphorescence') and that it is not further increased by bleaching. They thus  
686 proposed an optimum bleaching time of 800 s to reduce phosphorescence to its residual level  
687 without implementing an additional pause within the measurement procedure. However, this study  
688 contradicted the observation made on the same system (*Risø* TL/OSL DA-20 with IR-RF  
689 attachment) by Buylaert et al. (2012) who showed the appearance of IR phosphorescence even  
690 after bleaching of 1,500 s, though it was two orders of magnitude smaller than the IR-RF signal  
691 which can probably be considered negligible. Nevertheless, other studies contradicted these  
692 findings, e.g., Erfurt (2003b), Erfurt and Krbetschek (2003b) and Huot et al. (2015) showed the  
693 presence of phosphorescence directly emitted after bleaching. The above-described observations  
694 suggest that an additional pause of 30 min up to 1 h might be beneficial to minimize the potential

695 effects of unwanted signal superposition from the phosphorescence caused by bleaching (also Sec.  
696 5.3).

697 *Preheat and measurement temperature:* The work of Trautmann (1999) gave evidence for a strong  
698 temperature dependence of the IR-RF signal of K-feldspar, which appears to be related to the  
699 sample's age (see also Erfurt, 2003b). Considering the dependency of the IR-RF signal intensity  
700 (Trautmann, 1999; Erfurt, 2003b; Frouin, 2014) on the preheat and measurement temperature,  
701 measurements under well-controlled temperature conditions appear advisable. However, due to  
702 technical limitations, measurements under controlled (elevated) temperature conditions have only  
703 been applied by Frouin et al. (2017). They suggested a preheat of 70 °C based on the observation  
704 of thermally assisted phosphorescence. Huot et al. (2015) advised that a temperature range of 70  
705 °C to 100 °C would be suitable. However, Erfurt and Krbetschek (2003b) neglected the need for  
706 any preheat prior to measurement following their observation of no change in IR-RF intensity from  
707 room temperature to 250 °C (cf. Fig. 2 in Erfurt and Krbetschek, 2003b). Nevertheless, a  
708 comparison of IR-RF ages with independent age control showed improvement in results when  
709 measurements are carried out at elevated temperature (Frouin et al., 2017). Therefore, Frouin et al.  
710 (2017) recommended measurements at elevated temperature.

711 *Sensitivity correction (also Sec. 5.4):* Monitoring changes in the dose-response characteristics is  
712 an essential feature of every OSL SAR protocol. Schilles (2002) and Varma et al. (2013) included  
713 treatments to correct for unwanted changes in IR-RF signal sensitivity by introducing a correction  
714 factor for IR-RF measurements. Murari et al. (2018) investigated a new way of correction. In this  
715 method, the shapes of IR-RF curves are matched by moving the  $RF_{nat}$  vertically along with  
716 horizontal sliding (Sec. 5.4 for sensitivity change). This method was able to recover a given dose  
717 with 3–10 % accuracy, compared to an offset by 15–23 % when recovered only using the  
718 horizontal sliding method proposed by Buylaert et al. (2012). The recommended method (Kreutzer  
719 et al., 2017; Murari et al., 2018) does not need any extra measurements other than those  
720 implemented in the protocol suggested by Frouin et al. (2017). However, the  $RF_{nat}$  measurement  
721 should be long enough to produce an RF signal with pronounced curvature to match the  $RF_{nat}$  and  
722  $RF_{reg}$  curves.

723 **6.2 Data analysis**

724 Data analysis for  $D_e$  estimation is essential for age determination.  $D_e$  determination requires a  
725 comparison of the natural and a minimum of one regenerated IR-RF signal. The different methods  
726 available for making this comparison are described below.

727 ***Figure 11***

728 ***( $D_e$  determination methods)***

729 *Extrapolation and Interpolation method:* Three different approaches were presented to analyse IR-  
730 RF data (Fig. 11): (I) extrapolation, (II) interpolation and (III) sliding. The first two approaches  
731 comprise a mathematical curve fitting for  $D_e$  determination. Extrapolation (Fig. 11A) and  
732 interpolation (Fig. 11B) requires that either the natural or regenerative signal is recorded over a  
733 more extended period (natural signal: extrapolation; regenerative signal: interpolation). The  
734 chosen channel resolution and stimulation time determine the precision of the curve fitting and  
735 thus, the statistical error of the  $D_e$ . For curve fitting (extrapolation, interpolation), Trautmann et al.  
736 (1999a), Krbetschek et al. (2000) and Schilles (2002) proposed a single exponential decaying  
737 function with three parameters. Later, Erfurt and Krbetschek (2003b) recognized that the curve  
738 shape could be best described using a so-called stretched exponential function (Fig. 12). This  
739 function was suggested in a general form by, e.g., Pavesi and Ceschini (1993). The stretched  
740 exponential function introduces a dispersion factor ( $\beta$ ), which accounts for the underlying physical  
741 processes in disordered condensed matter systems. Unfortunately, the mathematical expression of  
742 this function type is not consistent in the IR-RF literature (Fig. 12) and differs regarding the  
743 placement of  $\beta$  in the equation. Although the functions shown in Fig. 12 may result in consistent  
744  $D_e$  estimations, they reveal different curve shapes for similar parameter sets. Therefore, parameters  
745 describing an IR-RF curve's decay cannot be compared without a statement on the applied  
746 mathematical expression.

747 ***Figure 12***

748 ***(Equations used for IR-RF curve fitting)***

749 Due to the general difficulties associated with  $D_e$  estimation by extrapolation (i.e., substantial  
750 uncertainties), this methodological approach appears to have been abandoned in later studies, and

751 more recently only  $D_e$  estimation by interpolation has been applied (e.g., Wagner et al., 2010;  
752 Novothny et al., 2010; Kreutzer et al., 2014). Nevertheless, every fitting method requires an  
753 assumption regarding the IR-RF curve shape, either based on a model or the best graphic adaption  
754 of the curve shape. Furthermore, IR-RF curves recorded only for a short time do not sufficiently  
755 reveal the curve shape and potential changes.

756 *Sliding method:* Buylaert et al. (2012) suggested a data analysis method based on horizontal sliding  
757 of the  $RF_{\text{nat}}$  curve until the best match is reached (inspired by the *Australian slide* method  
758 introduced initially by Prescott et al., 1993). This approach appears to be even more justified since  
759 Frouin et al. (2017) pointed out an initial rise at the beginning of the natural IR-RF curve (Sec.  
760 5.5). The observed initial rise at the beginning of the IR-RF curve does not allow an unbiased  
761 channel selection if curve fitting combined with interpolation or extrapolation is applied. In other  
762 words, for IR-RF data analysis, the (horizontal) sliding technique should be favoured over the  
763 curve fitting approach. However, it was often seen that  $RF_{\text{nat}}$  and  $RF_{\text{reg}}$  curves did not match after  
764 horizontal sliding. Kreutzer et al. (2017) suggested enhancing the technique by combining vertical  
765 and horizontal sliding to account for an observed IR-RF light level change encountered for a  
766 particular technical setup, presented in Murari et al. (2018). The sliding method requires a long  
767 natural IR-RF measurement to match the regenerative IR-RF, e.g., Frouin et al. (2017) (their  
768 supplement) recommended a minimum of 40 channels for robust  $D_e$  estimation for the horizontal  
769 sliding method. In the case of the vertical and horizontal sliding methods, Murari et al. (2018) used  
770 100 channels. However, the precise number depends on the signal shape.

771 *Error estimation:* Krbetschek et al. (2000) suggested that the primary source of random error in  
772 the IR-RF ‘mean’  $D_e$  arises from changes in the sample geometry at a single-grain level (see also  
773 Trautmann et al., 2000b). In contrast to OSL, where the dose-response curve is typically  
774 reconstructed with a few (e.g., 5–15) regenerative dose measurements, the number of channels  
775 used for constructing the IR-RF dose-response curve can be increased dramatically (e.g., >1,000  
776 values) and is limited only by the instrumental signal-to-noise ratio and the total number of allowed  
777 channels by the system. Consequently, for IR-RF dating studies, individual (statistical) errors have  
778 been ignored, and the standard error deduced from individual  $D_e$  distributions (e.g., Wagner et al.,  
779 2010; Lauer et al., 2011; Kreutzer et al., 2014). To account for potential errors Frouin et al. (2017)  
780 (their supplement) developed an approach to estimate the standard error of an individual aliquot

781 based on a non-parametric bootstrapping approach (Efron, 1979) for the sliding method.  
782 Nevertheless, the results of Frouin et al. (2017) also showed that the obtained individual statistical  
783 standard error remains negligible in comparison to inter-aliquot scatter and becomes relevant only  
784 for dim IR-RF signals.

785 *Data analysis software:* To analyse IR-RF data, no specialized software is needed, and commercial  
786 software solutions, e.g., *SigmaPlot*<sup>TM</sup> or *ORIGIN*<sup>TM</sup> may be sufficient to analyse single  
787 measurements. However, within a dating study, the amount of data may demand more  
788 comprehensive and efficient solutions. Two freely available software solutions have been  
789 published to analyse IR-RF data based on the IRSAR Erfurt and Krbetschek (2003b) approach.  
790 The *MS Windows*<sup>TM</sup> software *RLanalyse* (Lapp et al., 2012; latest version 1.20) has implemented  
791 the (horizontal) sliding method and works with BIN/BINX-files produced by a *Risø* TL/OSL  
792 reader. The most recent version of the function `analyse_IRSAR.RF()` implemented in the  
793 package ‘Luminescence’ (Kreutzer et al., 2012, 2018c) makes use of the platform-independent  
794 programming language **R** (R Core Team, 2018), and supports the horizontal and vertical sliding  
795 approach. The function also supports  $D_e$  estimation via curve fitting as described by Erfurt and  
796 Krbetschek (2003b) as well as via sliding including the individual standard error estimation  
797 approach described in Frouin et al. (2017) and Murari et al. (2018). Through the ‘Luminescence’  
798 environment, XSYG-files (Freiberg Instruments *lexsyg* readers), BIN/BINX-files (*Risø* TL/OSL  
799 reader) as well as various other data formats (e.g., file endings \*.csv, \*.txt) are supported as input  
800 data.

## 801 **7 Application of IR-RF dating**

802 The broader use of IR-RF as a dating method for sediments started mainly after introducing the  
803 IRSAR protocol by Erfurt and Krbetschek (2003b). Signal saturation levels of  $> 1,000$  Gy (e.g.,  
804 Erfurt and Krbetschek, 2003b and Sec. 5.7) favoured IR-RF dating applications on Middle  
805 Pleistocene sediments which are generally beyond the quartz OSL dating limit. The typical dose  
806 saturation for quartz OSL measured in the UV is reached around 150–200 Gy (Wintle and Murray,  
807 2006) except for a few cases where quartz doses  $>300$  Gy are reported (e.g., Lowick and Valla,  
808 2018). Until now, IR-RF dating has mainly been applied to coarse grain K-rich feldspar using  
809 multiple-grains (Secs. 7.17.2). Spatially resolved and single grain studies are limited to preliminary

810 work (e.g., Schilles 2002; Trautmann et al., 2000b) and a manuscript in an open discussion by  
811 Mittelstrass and Kreutzer (preprint) and are thus not further discussed here. Applications of IR-RF  
812 on polymineral fine-grain samples (4–11  $\mu\text{m}$ ) are currently limited to three studies (Schilles, 2002;  
813 Kreutzer et al., 2018b; Coussot et al., 2019).

## 814 **7.1 Application to glacio-fluvial and fluvial sediments**

815 In the past, IR-RF dating has been favoured particularly for constraining the timing of the Saalian  
816 glacial cycle and the Eemian interglacial by dating fluvial deposits of sites located in  
817 Central/Eastern Germany (Eissmann, 2002) by Degering and Krbetschek (2007), Krbetschek et al.  
818 (2008) and Kreutzer et al. (2014). Degering and Krbetschek (2007) presented IR-RF ages ranging  
819 from  $120 \pm 15$  ka to  $158 \pm 21$  ka for the Eemian site Klinge (Germany), and the results were in  
820 good agreement with quartz and K-feldspar OSL and IRSL luminescence dating results. IR-RF  
821 dated fluvial sites (e.g., Wallendorf and Delitzsch, Germany) are highly relevant for establishing  
822 a chronology for Middle Pleistocene Palaeolithic human activity in Europe due to the presence of  
823 stone-artefacts embedded in fluvial sands and gravels. Krbetschek et al. (2008) presented IR-RF  
824 ages ranging from  $\sim 150$  ka to  $\sim 306$  ka for the Saalian period and highlighted human activity in  
825 Central Germany already at around 300 ka. Lauer and Weiss (2018) compared pIRIR<sub>290</sub>  
826 luminescence ages from the important palaeolithic site of Markkleeberg (Baumann et al., 1983;  
827 Schäfer et al., 2003) with previously available IR-RF ages (Krbetschek et al., 2003) and found the  
828 pIRIR<sub>290</sub> and IR-RF ages were in excellent agreement and provided late MIS 6 ages for the upper  
829 fluvial sequence at the site. Also, for the key site of the *Homo heidelbergensis*, located at Mauer  
830 in south-west Germany, IR-RF was applied to fluvial deposits correlated to the archaeological  
831 horizon of the Mauer mandible. At this site, the IR-RF ages were in good agreement with results  
832 of combined electron spin resonance (ESR)/U-series dating on mammal teeth, yielding an age of  
833 around 0.6 Ma (Wagner et al., 2010). Lauer et al. (2011) used IR-RF to date fluvial deposits  
834 collected from sediment-cores drilled into the northern Upper Rhine Graben (Germany). They  
835 deduced several fluvial aggradation periods and phases of increased tectonic subsidence between  
836  $\sim 300$  ka and  $\sim 650$  ka based on these IR-RF ages. Li et al. (2017) compared the data reported by  
837 Lauer et al. (2011) with their chronology based on fading corrected pIRIR<sub>225</sub> ages obtained for the  
838 core Heidelberg UniNord 1. Except for the lowermost sample (below the B/M boundary) both  
839 chronologies were broadly consistent. For the lowest sample, Li et al. (2017) reported a minimum

840 age of  $>602 \pm 77$  ka, consistent with the magnetostratigraphic information which was not available  
841 in 2011. In light of the new findings, the IR-RF age of  $643 \pm 28$  ka by Lauer et al. (2011) should  
842 be considered as minimum age. The reasons for this age underestimation should be subject to  
843 future research.

844 In general, studies presented by Krbetschek et al. (2008) and Wagner et al. (2010) demonstrated  
845 good agreement with independent age control. In contrast to these studies, Buylaert et al. (2012)  
846 showed that IR-RF dating results of coastal marine sediments from Russia and Denmark as well  
847 as colluvial sediments from France were either overestimated (for ages between 20–45 ka) or  
848 underestimated (for older samples  $\sim 128$  ka) compared to independent dating methods based on  
849 biostratigraphy, radiocarbon ( $^{14}\text{C}$ ), OSL and pIRIR<sub>290</sub> (for numerical values cf. Table S1 in  
850 Buylaert et al., 2012).

851 *Figure 13 ABC*

852 *(Age comparison)*

853 **7.2 Application to aeolian deposits**

854 Well-bleached sediments, such as wind-blown loess or dune sands seem to be most suitable for  
855 IR-RF dating applications, although the amount of sand-sized K-feldspars in silt-dominated loess  
856 is limited. Early aeolian samples used for IR-RF dating result originate from a sediment core from  
857 the Gaxun Nur Basin in North-West Chin (Wünnemann et al., 2007). The IR-RF dating results<sup>2</sup>  
858 significantly overestimated previously reported TL/IRSL ages and were discarded by the authors  
859 (Wünnemann et al., 2007), without presenting further technical details.

860 Novothny et al. (2010) were the first to extract coarse-grained K-feldspars from Hungarian loess  
861 for IR-RF dating. The IR-RF ages of  $\sim 200$  ka presented by Novothny et al. (2010) significantly  
862 overestimated the fading-corrected IRSL ages of  $\sim 130$  ka, explained due to insufficient bleaching  
863 of the coarse-grained fraction. An IR-RF age overestimation compared to quartz OSL ages of  
864 reworked aeolian sediments from Egypt was also reported by Buylaert et al. (2012), which was  
865 either attributed to a preliminary determination of the bleaching level before the regenerative dose

---

<sup>2</sup> In Fig. 22.3 (Wünnemann et al., 2007) the IR-RF results were erroneously presented as OSL dates.



866 measurement or sensitivity changes between the measurement of the natural and regenerated  
867 curves.

868 It was recently demonstrated that the modified IRSAR-protocol, measuring the IR-RF signal at  
869 70 °C (RF<sub>70</sub>), recovered IR-RF ages on modern aeolian samples that agreed with independent age  
870 control. Frouin et al. (2017) have shown reasonable agreement with independent age control from  
871 polymineral (4–11 µm) fine-grain results published by Meszner et al. (2013). However, they also  
872 observed a large scatter in their  $D_e$  distributions. Another age from a loess sample from the same  
873 site appeared to be underestimated. This offset was explained by the low  $D_e$  values resulting from  
874 low signal intensities (Frouin et al., 2017).

875 Kreutzer et al. (2018a) presented a dating application study on coastal dynamics from the Médoc  
876 region (south-west France), comparing coarse grain K-feldspar IR-RF ages (RF<sub>70</sub> protocol) with  
877 quartz OSL ages and quartz multiple-centre ESR dating (Toyoda et al., 2000). In this study, the  
878 IR-RF ages were systematically older than the SAR quartz ages, which was believed to be a  
879 consequence of insufficient resetting of the IR-RF signal. However, this study showed reasonable  
880 agreement with the ESR ages for older sediments (200–330 ka). Similarly, Scerri et al. (2018) also  
881 found that RF<sub>70</sub> and pIRIR<sub>290</sub> age estimates were consistent within a 2-sigma limit and in  
882 stratigraphic order. The aeolian samples from an archaeological site in Saudi Arabia resulted in  
883 age estimates of ~276 ka for the older (archaeologically sterile) layer and 197 ka for the human  
884 occupation layer.

### 885 **7.3 Remarks on IR-RF age accuracy and independent age control**

886 Figure 13 presents a non-exhaustive overview of published IR-RF data. The ages from the IR-RF  
887 dating approaches generally show good agreement with independent age control (e.g., Degering  
888 and Krbetschek, 2007), whereas the IR-RF ages from Buylaert et al. (2012) disagree with  
889 independently derived ages. Again, a good agreement between IR-RF and independent ages was  
890 reported using a modified IRSAR protocol (RF<sub>70</sub>) suggested by Frouin et al. (2017).

891 The study by Frouin et al. (2017) was the first to present various IR-RF dating applications with a  
892 modified IRSAR protocol (RF<sub>70</sub>), which agreed with independent age control. IR-RF dating of a  
893 Pleistocene beach deposit from Peru and colluvial deposits from France appeared to be  
894 overestimated compared to independent age information from IRSL, U/Th series or radiocarbon

895 dating; a pattern also observed by Schaarschmidt et al. (2019). However, for the Peruvian sample,  
896 IR-RF and pIRIR<sub>290</sub> ages agreed within error limits. Similarly, Holocene beach sand from  
897 Denmark and another colluvial example from France yielded ages in good agreement with  
898 independent age information. In conclusion, published IR-RF dating results indicated that the IR-  
899 RF dating method produced correct ages in some cases, but fails for other cases. It seems that there  
900 are still methodological problems related to IR-RF dating, and further investigation is needed to  
901 overcome these challenges.

## 902 **8 Summary and future directions of IR-RF dating**

903 Overall, regardless of ambivalent dating results in some studies, IR-RF appears to be a promising  
904 but somewhat overlooked dating method on K-feldspars. The status quo renders a picture with  
905 several, potentially, game-changing advantages but without a significant breakthrough because  
906 those benefits are not received as significant enough by dating practitioners. On the other hand,  
907 IR-RF poses a bunch of open questions and challenges that are yet to overcome.

### 908 **8.1 The status quo**

909 The plus side of IR-RF dating has different dimensions. From a **methodological perspective**, IR-  
910 RF is believed to monitor the trapping of electrons in the principal trap, i.e., it is a *direct*  
911 measurement of the dose accumulation in the mineral. This approach is conceptionally different  
912 from conventional OSL, IRSL and TL measurements, involving secondary recombination  
913 processes to infer the signal of interest. Debated methodological issues, such as phosphorescence  
914 and sensitivity change (see Secs. 5.35.4), appear to be manageable by proper experimental and  
915 data analysis design.

916 From a **practical perspective**, compared to post-IR IRSL dating, for instance, the measurement  
917 sequence for one aliquot is reasonably concise, less error-prone, and, depending on the aimed dose  
918 range, likely less time-consuming (depending on the chosen measurement sequence). The dose-  
919 response curve is the IR-RF curve measured during irradiation with a resolution usually in the  
920 order of a fraction of a Gy. Instead of applying different fitting equations determining the  $D_e$ , the  
921 data analysis using the sliding method, i.e., matching two dose-response curves ( $RF_{nat}$  and  $RF_{reg}$ ),  
922 could not be more straightforward. Software to analyse IR-RF signals is freely available and partly

923 open-source. The biggest obstacle for applying IR-RF dating in the past, availability of equipment,  
924 is no more. At least two commercial manufacturers offer ready-to-use IR-RF readers for research  
925 and dating applications.

926 From a **dating perspective**, the target mineral, K-feldspar, shows a high natural abundance, an  
927 acknowledged higher luminescence dating range compared to quartz, and the internal potassium  
928 concentration lowers the impact of the external dose-rate contribution. However, conventional  
929 feldspar luminescence is reported to suffer from an unwanted athermal signal loss (fading).  
930 Contrary to IRSL, no definite evidence was provided for fading of the IR-RF signal of K-feldspars  
931 to date. Although Buylaert et al. (2012) reported age underestimations for older samples of ca  
932 30 %, this does not appear to be a generally observed pattern. Furthermore, signal instability as a  
933 cause for this observation was considered unlikely by Kumar et al. (2021). The thermal stability  
934 of the IR-RF signal (determining the potential age range) appears to be sufficiently high up to  
935 700 °C (Sec. 5.6), though previous experiments indicated changes of the IR-RF signal shape above  
936 ~250 °C (Trautmann et al., 1999a; Erfurt and Krbetschek, 2003b; Frouin et al., 2017).

937 However, to sustain, a dating method has to show advantages over established methods, which are  
938 also perceived as significant for application studies. Supposing that the signal of choice is  
939 thermally and athermally stable, for luminescence-based chronologies such advantages are  
940 measured in terms of bleachability and temporal range.

941 Compared to pIRIR<sub>290</sub>, which seems to suffer from no or at least less fading than IRSL, IR-RF's  
942 bleachability is comparable. In other words, in natural environments involving sediment transport  
943 processes with only short sunlight exposure, IR-RF dating seems to be as applicable as pIRIR<sub>290</sub>  
944 and other methods may suit better. Whether the temporal range is as high as the ~1.2–3 Ma (~  
945 3,600 Gy) postulated by Murari et al. (2018) is yet to be revealed. More realistically seem values  
946 around up to 1,500 Gy measured by, e.g., Erfurt (2003b), Frouin (2014), Frouin et al. (2017) and  
947 Kreutzer et al. (2018). Here we conclude that the signal saturation limit (and thus the temporal  
948 range) appears to be significantly higher than for conventional OSL on quartz (up to 400 Gy,  
949 typically lower, for a review cf. Wintle and Adamiec, 2017). This “winning margin” is less  
950 pronounced if IR-RF is compared to studies reporting post-IR IRSL (more specific: pIRIR<sub>290</sub>) or  
951 MET-pIRIR results. For instance, Liu et al. (2016) reported doses up to ca. 1,240 Gy, however,

952 ages were reported to underestimate the independent age control above ca. 600–900 Gy (cf. Lieu  
953 et al., 2016; their Table 2 and Fig. 3). For MET-pIRIR, Li et al. (2014) reported potential natural  
954 dose measurements up to ca. 1,500 Gy, however, it remains unclear whether such values can be  
955 met regularly in routine dating studies (cf. Zhang and Li, 2020 for a discussion).

## 956 **8.2 Future directions**

957 Future methodological research on IR-RF should first resolve some open debates, particularly on  
958 signal saturation and signal stability (fading). Although fading does not appear to be a generally  
959 observed pattern, this topic should be explored in more detail, along with potential sensitivity  
960 changes using samples of known and geological age. The biggest obstacle to resolving whether  
961 the signal recorded with IR-RF is stable or suffers from an athermal signal loss over geological  
962 timescales might be the experimental design. From the current perspective, it appears that short  
963 experiments over a couple of weeks to months are not sufficient to provide answers to that  
964 question. Hence, research should involve laboratories with a relatively long history and an archive  
965 of already measured, irradiated and stored feldspar specimen. The quantification of the saturation  
966 level is more of theoretical than practical relevance.

967 With regard to the literature, it is safe to assume a rather broad, sample dependent, saturation level  
968 range between 600 Gy and 2,000 Gy up to perhaps 4,000 Gy. However, of relevance for the dating  
969 practice is the limit of the K-feldspar sample at hand, regardless of any theoretical value. In other  
970 words, the saturation level of IR-RF dating and with it the temporal range, will itself establish  
971 circumstantially over time; with or without dedicated research. However, both research on the  
972 fading behaviour and the signal saturation might contribute to a broader understanding of the  
973 physics underpinning IR-RF. To date, Trautmann's model (Trautman et al., 2000a) remained, to  
974 our knowledge, the only comprehensible model genuinely dedicated to IR-RF. Clearly, efforts are  
975 needed to combine the old and new findings around IR-PL and combine them with established  
976 knowledge in IRSL to decipher the proposed resemblance of IR-RF and IR-PL (cf. Kumar et al.,  
977 2020). Similarly, while there seems to be extensive research to identify the defect responsible for  
978 IR-PL (most recently Kumar et al., 2020), it appears that established knowledge on the role of Pb  
979 in the luminescence production in feldspar (cf. textbook by Ostrooumov, 2016) did not (yet)  
980 receive full attention.

981 On the application site, the next logical application step is spatially resolved IR-RF in a single  
982 grain (Mittelstrass and Kreutzer, preprint) or even sub-grain level as concluded by Kumar et al.  
983 (2020).

984 Another direction to test, for already available multi-grain IR-RF, are fine-grain (polyminerale)  
985 mineral fractions. The few attempts reported in the literature yielded promising results (Schilles  
986 2002; Coussot et al., 2019). However, the mixture of minerals in such samples may hamper its  
987 application. Meyer et al. (2013) used quantitative evaluation of minerals by scanning electron  
988 microscopy (QEMSCAN) for polyminerale fine grain OSL samples from interglacial lacustrine  
989 units (NW11 and THG 4 from Switzerland; Lowick et al., 2012) and found that K-feldspar  
990 amounts only to ~2–4 %. The major component of the samples was quartz (40–50 %). Tsukamoto  
991 et al. (2012) confirmed similar observations for various loess samples using X-ray diffractometry  
992 (XRD) as well as scanning electron microscopy-energy dispersive X-ray (SEM-EDX). While  
993 quartz samples emit RF in the IR region, but not beyond 735 nm (Schmidt et al., 2015), quartz  
994 may not interfere with the main IR-RF emission (865 nm). However, the polyminerale composition  
995 may lead to unfortunate emission spectra with, e.g., a dominating peak at 710 nm (cf. Heydari et  
996 al., 2021, for an unsuccessful IR-RF dating attempt using polyminerals). Hence, for such an  
997 application, spectrometer measurements appear indispensable. Besides, deploying IR-RF on  
998 polyminerale fine grain samples would significantly broaden the application to environmental  
999 settings where grain sizes <90 µm dominate, and applications can be tested preferably without  
1000 extensive methodological research.

1001 In summary, the current status of IR-RF dating still leaves room for rich methodological and  
1002 application studies towards a potentially bright future.

### 1003 **Acknowledgements**

1004 We are grateful to Sébastien Huot, Frank Preusser and two anonymous reviewers for their patience,  
1005 constructive comments, and strong support for this manuscript. M.K. Murari and M. Fuchs were  
1006 supported by the German Research Foundation (DFG FU417/19-1). S. Kreutzer and N. Mercier  
1007 received financial support by the LaScArBx. LaScArBx is a research programme supported by the  
1008 ANR (ANR-10-LABX-52). The contribution of S. Kreutzer in 2020 received funding from the  
1009 European Union's Horizon 2020 research and innovation programme under the Marie

1010 Skłodowska-Curie grant agreement No 844457 (CREDit). M. Frouin was supported by the John  
1011 Fell Fund (161/067 and 171/006) University of Oxford. N. Klasen received funding by the  
1012 Deutsche Forschungsgemeinschaft (DFG, German Research Foundation) – Project number  
1013 57444011 – CRC 806 "Our way to Europe ". All authors thank L. Diehl for drawing Figure 3.

1014

1015 **Figure captions**

1016 **Figure 1**

1017 Schematic of the different luminescence transitions involved in IR-RF, IRSL and post-IR IRSL  
1018 measurements, based on Trautmann et al. (1998, 1999a, 2000a) and Jain and Ankjærgaard (2011).  
1019 Colours read as follows: Black lines indicate electron transitions; blue lines indicate hole  
1020 migrations. Red colours also refer to electron transitions but related to the production of IRSL.  
1021 [a] Exposure to ionizing radiation results in a constant flux of electrons from the valence band to  
1022 the conduction band. These electrons may recombine radiatively [b], non-radiatively (not-shown  
1023 for clarity), drop immediately back to the valence band (not-shown for clarity) or populate the  
1024 IRSL trap [c]. Electrons that populate the IRSL trap pass through the excited state, resulting in  
1025 infrared radiofluorescence (1.43 eV). Electrons within the IRSL trap are sensitive to infrared light  
1026 and preferentially recombine with proximal holes. Additionally, the electrons may tunnel directly  
1027 from the ground-state of the trap [d] (anomalous fading). Alternatively, Trautmann (2000) and  
1028 Trautmann et al. (2000a) proposed hole production by allowing a direct transition of electrons into  
1029 the valence band. This facilitates new possibilities for the recombination of electrons in the IRSL  
1030 trap [e]. Note that each electron stimulated from the valence band will result in the production of  
1031 a hole. However, these are not shown for clarity. If the electrons are stimulated with infrared light,  
1032 they reach the excited state of the trap, from which they can migrate locally [f] before recombining.  
1033 Higher temperature stimulations provide phonon-assistance (dashed black arrows), allowing post-  
1034 IR IRSL signals to be measured from electrons that have diffused through the band-tail states to  
1035 more distal holes [g], which are thermally and athermally more stable.

1036 **Figure 2**

1037 Schematic representation of self-made and commercially available measurement devices. A) The  
1038 device used by Erfurt (redrawn after Erfurt et al., 2003). B) The device used by Schilles (redrawn  
1039 after Schilles, 2002). C) The device manufactured by *Risø* laboratories (redrawn after Lapp et al.,  
1040 2012). D) The device manufactured by Freiberg Instruments (redrawn after Richter et al., 2013)

1041

1042 **Figure 3**

1043 The efficiencies of four different spectrometers. The overall efficiencies of spectrometers were  
1044 approximated by multiplying the individual efficiencies of the grating with those of the  
1045 spectrograph and the CCD chip.

1046 **Figure 4**

1047 Effective detection band for (A) the setups used by Schilles (2002) and Erfurt (2003b), and (B)  
1048 *Risø* and *lexsyg research* readers. The net transitions were estimated by interpolation and by  
1049 multiplying the filter transmission and quantum efficiency of the PMT.

1050 **Figure 5**

1051 Simulated Gaussian IR-RF peaks from K-feldspar at 710 nm, 865 nm and 910 nm (similar to Erfurt  
1052 and Krbetschek, 2003b). The main IR-RF peak is centred at 865 nm. A) Simulated IR-RF spectrum  
1053 with a high 865 nm peak, simulating a bleached sample. B) Simulated IR-RF spectrum with a high  
1054 710 nm peak, a situation appearing when the sample is dosed. C) A typical spectrum from K-  
1055 feldspar for a sediment sample (redrawn after Schilles, 2002).

1056 **Figure 6**

1057 IR-RF bleaching using different bleaching sources. A) Sunlight bleaching (redrawn after  
1058 Trautmann et al., 1999a). Full signal resetting is reached within 4–6 h. B) Monochromatic  
1059 bleaching for wavelengths <500 nm; a bleaching plateau seems to be reached within ca. 0.3 h  
1060 (redrawn after Trautmann et al., 2000a). C) Solar simulator (200 W high-pressure Hg-lamp, 5 mm  
1061 Schott KG3 heat absorbing filter at a distance 20 cm) allows full signal resetting within 0.7 h  
1062 (redrawn after Krbetschek et al., 2000). D) A bleaching comparison of IR-RF measured at elevated  
1063 temperature (RF<sub>70</sub>) with IR<sub>50</sub>, pIRIR<sub>225</sub> and pIRIR<sub>290</sub> (redrawn after Frouin et al., 2017). Resetting  
1064 of the IR-RF signal is much slower compared to IR<sub>50</sub> and pIRIR<sub>225</sub>, but it is similar or slightly  
1065 faster than pIRIR<sub>290</sub> and needs ~3 h bleaching time. The x-axis scale is similar for all subplots.

1066 **Figure 7**

1067 IR phosphorescence of a K-feldspar sample after bleaching as observed by Erfurt and Krbetschek  
1068 (2003b) (redrawn after Erfurt and Krbetschek, 2003b).



1069 **Figure 8**

1070 A schematic representation to explain the sensitivity change monitored by various authors using  
1071 different methods. A) Derived sensitivity correction factor ( $s$ ) by fitting exponential functions to  
1072 two bleached regenerated IR-RF ( $RF_{reg}$ ) curves (Schilles, 2002). B) Sensitivity correction factor  
1073 ( $F_s$ ) estimation using spline fitting and extrapolation (Varma et al., 2013). C) Sensitivity correction  
1074 of IR-RF data by sliding the natural IR-RF ( $RF_{nat}$ ) curve vertically up or down along with  
1075 horizontal sliding to find the best match with the  $RF_{reg}$  curve (see main text for detail).

1076 **Figure 9**

1077 A) A typical behaviour of the initial rise of IR-RF from a natural sample. The first few channels  
1078 of the measured data show an initial rise in IR-RF intensity before decaying monotonically. B) IR-  
1079 RF signal dynamic range measured while irradiating the sample with a cumulative dose of 3,900  
1080 Gy. The typical dynamic range of IR-RF signals is  $\sim 2$ , as reported by Schilles (2002) and (Erfurt,  
1081 2003b).

1082 **Figure 10**

1083 IR-RF signal stability with respect to pulse annealing temperature. A) All natural IR-RF ( $RF_{nat}$ )  
1084 signals measured for a fixed short duration at different annealing temperatures. All samples show  
1085 an increase in IR-RF up to 150 °C. For samples Gro8 and Es1 the signal decrease for temperatures  
1086  $> 250$  °C, but remains stable for sample Ook1, a  $>1$  Ma old sample (redrawn after Trautmann et  
1087 al., 1999a). B) The signal remains stable until ca 250 °C for  $RF_{nat}$  and regenerated IR-RF ( $RF_{reg}$ )  
1088 for sample TH8 and changes its intensity for temperatures  $>250$  °C (redrawn after Frouin et al.,  
1089 2017).

1090 **Figure 11**

1091 Graphical representation of IR-RF data analysis techniques used to determine the  $D_e$ . A) The  $D_e$  is  
1092 obtained by extrapolation using the fitted natural IR-RF signal. B) The natural IR-RF signal is used  
1093 to re-calculate the  $D_e$  using the fitted regenerated IR-RF curve after bleaching. C) The natural and  
1094 the regenerated IR-RF signals are recorded before both are matched via (horizontal) sliding. D)  
1095 The natural curve is moved up or down via vertically sliding to find both curves' best match. The  
1096  $D_e$  is defined as the offset of the natural signal on the x-axis (for further details, see main text).

1097 **Figure 12**

1098 Simulated IR-RF curves for different equations reported in the literature, with  $\Phi_0$  the initial IR-RF  
1099 photon flux,  $\Delta\Phi$  the dose-dependent change of the IR-RF flux,  $\lambda$  the decay parameter,  $\beta$  the  
1100 dispersion factor and  $D$  the dose. For similar parameter values, the curve shapes differ markedly.  
1101 Values chosen for the figure:  $\Phi_0 = 1$ ,  $\Delta\Phi = 1$ ,  $\lambda = 2.274\text{e-}03$ ,  $\beta = 7.6\text{e-}01$ .

1102 **Figure 13**

1103 A) Independent age control vs IR-RF age (redrawn after Degering and Krbetschek, 2007). All IR-  
1104 RF ages match within the error limits when compared to independent ages. B) All IR-RF ages  
1105 show either over or underestimation compared to independent age control (redrawn from  
1106 supplement data, Buylaert et al., 2012). C) Independent age control vs IR-RF ages measured with  
1107 a modified IRSAR protocol (RF<sub>70</sub>) (redrawn after Frouin et al., 2017). Almost all ages match  
1108 within  $2\sigma$  uncertainty. Abbreviations used in figure legends: IR-RF SOL2: IR-RF ages when  
1109 samples are bleached for 4 h using the external solar lamp Hönle SOL2, Biost.: Biostratigraphy,  
1110 IRSL-50<sub>fc</sub>: Fading corrected IRSL age.

1111

## **Table captions**

Table 1: The main emission bands and possible defects observed in feldspar (copyright by Prasad 2017, permission granted by the author).

Table 2: Irradiation source parameters for various devices used for IR-RF stimulation.

Table 3: The relevant parameters for different spectrometer configurations.

Table 4: Detection parameters for various devices used for IR-RF detection.

Table 5: Bleaching source parameters for various devices used for IR-RF bleaching.

Table 6: Overview of published IR-RF measurement protocols used for  $D_e$  determination.

Table 1:

<i>Emission band</i>	<i>Excitation</i>	<i>Possible origin</i>	<i>Reference</i>
~3.8–4.4 eV (280–320 nm)	TL	Strain and/or ionic diffusion	Garcia-Guinea et al. (1999)
	PL	Tl <sup>+</sup>	Gorobets et al. (1995)
	IRSL		Baril and Huntley (2003a)
	TR-OSL		Clark and Bailiff (1998)
~3.1 eV (400 nm)	CL	Paramagnetic defect	*Finch and Klein (1999)
	IRSL	?	Rieser et al. (1999)
	IRSL	?	Baril and Huntley (2003a)
~2.2 eV (560 nm)	IRSL	Mn <sup>2+</sup>	Rieser et al. (1997)
	IRSL		Baril and Huntley (2003a)
	CL		Geake et al. (1977)
	TR-OSL		Clark and Bailiff (1998)
~1.7 eV (730 nm)	Absorption	Fe <sup>3+</sup>	White et al. (1986)
	PL		Telfer and Walker (1975)
	IRSL		Krbetschek et al. (1997)
	PL		Poolton et al. (1996, 2006)
~1.45 eV (855 nm)	RL or RF	IRSL dating trap	Trautmann et al. (1998)
~1.41–1.3 eV (900 nm) (~880 nm and ~955 nm)	CL (at 7 K)	IRCL trap with two sites and Fe <sup>4+</sup> as a competitor	Kumar et al. (2020)
~1.3–1.36 eV (910 nm)	RL or RF	Pb <sup>+</sup>	Erfurt (2003b)
	Post IR phosphorescence	IRSL dating trap	Baril and Huntley (2003a)
	TL	?	Krbetschek and Rieser (1995)

TL: Thermoluminescence, IRSL: Infrared stimulated luminescence, CL: Cathodoluminescence, RF: Radiofluorescence, RL: Radioluminescence, PL: Photoluminescence

TR-OSL: Time-resolved optically stimulated luminescence, IRCL: Infrared Cathodoluminescence

\* Finch and Klein (1999) reported the peak maximum at 430 nm related to Al<sup>3+</sup>-O<sup>2-</sup>-Al<sup>3+</sup> “Löwenstein” bridges.

Table 2:

<i>Laboratory / Manufacturer</i>	<i>Radiation source</i>	<i>Activity [GBq]</i>	<i>Radiation Type</i>	<i>Source type</i>	<i>Dose rate [Gy min<sup>-1</sup>]</i>	<i>Active area [mm<sup>2</sup>]</i>	<i>Reference</i>
Freiberg	<sup>137</sup> Cs/ <sup>137</sup> Ba	0.0037	β and γ	Planar	0.050	19.6	Trautmann (1999)
Freiberg	<sup>137</sup> Cs/ <sup>137</sup> Ba	0.0050	β and γ	Planar	0.080	50.3	Erfurt (2003b)
Heidelberg	<sup>137</sup> Cs/ <sup>137</sup> Ba	0.0037	β and γ	Planar	0.034	28.3	Schilles (2002)
Risø	<sup>90</sup> Sr/ <sup>90</sup> Y	1.48	β	Planar	2.640	50.3	Buylaert et al. (2012)
Freiberg Instruments	<sup>90</sup> Sr/ <sup>90</sup> Y	1.6–2	β	Ring	2.250	n.a.	Richter et al. (2012)

# Erfurt calibrated the radiation source with Al<sub>2</sub>O<sub>3</sub>:C while the other readers were calibrated with natural (calibration) quartz.

Table 3:

<i>Laboratory / Manufacturer</i>	Spectrograph	<i>Spectrograph/Grating</i>		Dispersion [nm]	Company	<i>CCD Camera</i>			<i>Reference</i>
		Grating	Blazed			Camera type	Active Pixels	Cooling Type	
Freiberg	Jobin Yvon CP200	Holographic	Not applicable	300–1000	Marconi	NA	1152x298	-100 °C (Liquid nitrogen)	Rieser et al. (1994)
Freiberg	Jobin-Yvon CP200	Holographic	Not applicable	250–1152	Marconi	Front-illuminated	1152x352	-100 °C (Liquid nitrogen)	Erfurt (2003b), Rieser et al. (1994)
Heidelberg	Acton SP150	150 lines/mm	300 nm	200–1100	Princeton Instruments	Back-illuminated	1100x330	-100 °C (Liquid nitrogen)	Rieser et al. (1999)
Freiberg Instruments	Andor Shamrock 163	300 lines/mm	500 nm	200–1050	Andor Newton 920-BU/iDus 420 OE	Back-illuminated / Open Electrode	1024x255	-80 °C (TE Cooled)	Richter et al. (2013)

TE Cooled: Thermoelectric cooling

Table 4:

<b>Laboratory/ Manufacturer</b>	<b>Detector</b>	<b>Detection [nm]</b>	<b>Filters</b>	<b>Bandpass [nm]</b>	<b>Light collection</b>	<b>References</b>
Freiberg	Spectrometer	300–1000	No filter	300-1000	Optical Guide	*Trautmann (1999)
Freiberg	Spectrometer / Hamamatsu (R943-02)	160–930	HQ865/20	855-875	Optical Guide	#Erfurt (2003b)
Heidelberg	Spectrometer / Hamamatsu (R943-02)	160–930	IR83 HOYA	820-930	Optical Guide	#Schilles (2002)
Risø	Hamamatsu (H7421-50)	380–890	Chroma D900/100	850-890	Optical Guide	Buylaert et al. (2012)
Freiberg Instruments	Spectrometer / Hamamatsu (H7421-50)	380–890	Chroma D850/40	845-885	Direct	Richter et al. (2013)

\*Trautmann's research was based on spectrometer measurements using a 200–800 nm detection range. Later, the spectrometer was modified for detecting 300–1,000 nm. The integrated counts of IR-RF peak were used to estimate the  $D_e$ .

#Schilles and Erfurt used liquid-cooled thermoelectric housing (LCT50, Thorn EMI) at about -20 °C to reduce the thermal noise.

Table 5:

<i>Laboratory/ Manufacturer</i>	<i>Bleaching source</i>	<i>Spectrum</i>	<i>Max Power*</i> <i>[mW cm<sup>-2</sup>]</i>	<i>Connection</i>	<i>Reference</i>
Freiberg	Hg-Lamp	UV-VIS	--	Optical Guide	# Trautmann (1999)
Freiberg	250W OSRAM LAMP	UV-VIS	100	Optical Guide	+Erfurt (2003b)
Heidelberg	150W QTH	UV-VIS	80	Optical Guide	+Schilles (2002)
Risø	UV LED	UV	700	Direct	Buylaert et al. (2012)
Freiberg Instruments	6 LED solar simulator	UV-IR	700	Direct	Richter et al. (2013)

\*Maximum power density of the bleaching units refers to approximate power at the sample position. It can vary from device to device.

#Trautmann (1999) used an interference filter in front of the solar lamp for monochromatic bleaching.

+Schilles (2002) and Erfurt (2003b) both used an IR cut-off filter.



1 Table 6:

Reference	Protocol Abbr.	Treatments and observations <sup>1</sup>						Data analysis	Comments
		#1	#2	#3	#4	#5	#6		
Buylaert et al. (2012)	NA (based on IRSAR)	-	IR-RF [ $RF_{nat}$ ]	Bleaching ( $\geq 1,800$ s) (ca. 395 nm)	Pause ( $\geq 3,600$ s)	-	IR-RF [ $RF_{reg}$ ]	Sliding	-
Erfurt and Krbetschek (2003b)	IRSAR	-	IR-RF [ $RF_{nat}$ ]	Bleaching ( $\geq 1,800$ s) (artificial solar spectrum)	Pause ( $\geq 3,600$ s)	-	IR-RF [ $RF_{reg}$ ]	Fitting (interp.)	$RF_{nat}$ is represented by only a few channels
Frouin et al. (2017)	$RF_{70}$ (based on IRSAR)	PH@70 °C (900 s)	IR-RF@70 °C [ $RF_{nat}$ ]	Bleaching@70 °C ( $\geq 7,200$ s) (artificial solar spectrum)	Pause ( $\geq 3,600$ s)	PH@70 °C (900 s)	IR-RF@70 °C [ $RF_{reg}$ ]	Sliding	-
Krbetschek et al. (2000)	NA	-	IR-RF [ $RF_{nat}$ ]	Bleaching ( $\geq 1,800$ s) (artificial solar spectrum)	-	-	IR-RF [ $RF_{reg}$ ]	Fitting Sliding	Based on the results by Trautmann et al. (1999a), but with artificial bleaching
Trautmann et al. (1999a)	NA	-	IR-RF [ $RF_{nat}$ ]	Bleaching (natural sunlight)	-	-	IR-RF [ $RF_{reg}$ ]	Fitting (extrapol.)	$RF_{reg}$ is represented by only a few channels
Schilles (2002)	NA	-	IR-RF [ $RF_{nat}$ ]	Bleaching $\geq 3,600$ s) (artificial solar spectrum)	Pause ( $\geq 1,800$ s)	-	IR-RF [ $RF_{reg}$ ]	Fitting	Combination of extrapolation and interpolation for the data analysis; sensitivity correction using a separate aliquot (Schilles, 2002, p. 97)
Varma et al. (2013) <sup>2</sup>	NA (based on IRSAR)	-	IR-RF [ $RF_{nat}$ ]	Bleaching ( $\geq 800$ s) (ca. 395 nm)	-	-	IR-RF [ $RF_{reg}$ ]	Sliding	200 s phosphorescence measurement before and after each IR-RF measurement; Repeat step #3 and #6 to monitor sensitivity changes

2 <sup>1</sup>The instrumental setup differs considerably across the studies and should be considered before protocol application. If no measurement temperature is listed, such value was not  
3 reported by the study or no additional heating above ambient temperature was applied. Please note that the table lists only general treatments, for further details the reader is referred  
4 to the respective publication.

5 <sup>2</sup>The authors used their protocol for dose recovery tests only; distinct  $D_e$  determinations are not mentioned.

6 PH: Preheat | NA: Not available

7

8

## 9 References

- 10 Aitken, M.J., 1985a. Thermoluminescence dating. Academic Press.
- 11 Aitken, M.J., 1985b. Alpha particle effectiveness: numerical relationship between systems.  
12 Ancient TL 3, 22–25.
- 13 Aitken, M.J., 1998. An introduction to optical dating. Oxford University Press.
- 14 Auclair, M., Lamothe, M., Huot, S., 2003. Measurement of anomalous fading for feldspar IRSL  
15 using SAR. Radiation Measurements 37, 487–492. doi:10.1016/S1350-4487(03)00018-0
- 16 ASTM International, 2012. ASTM G173-03(2012) Standard Tables for Reference Solar Spectral  
17 Irradiances: Direct Normal and Hemispherical on 37° Tilted Surface, ASTM International,  
18 West Conshohocken, PA. <http://www.astm.org>. doi: 10.1520/G0173-03R12
- 19 Baril, M.R., Huntley, D.J., 2003a. Optical excitation spectra of trapped electrons in irradiated  
20 feldspars. J. Phys.: Condens. Matter 15, 8011–8027. doi: 10.1088/0953-8984/15/46/017.
- 21 Baril, M.R., Huntley, D.J., 2003b. Infrared stimulated luminescence and phosphorescence spectra  
22 of irradiated feldspars. J. Phys.: Condens. Matter 15, 8029–8048. doi: 10.1088/0953-  
23 8984/15/46/018.
- 24 Baumann, W., Mania, D., Toepfer, V., Eißmann, L., 1983. Die paläolithischen Neufunde von  
25 Markkleeberg bei Leipzig. Landesmuseum für Vorgeschichte Dresden 16.
- 26 Brooks, R.J., Finch, A.A., Hole, D.E., Townsend, P.D., Wu, Z.-L., 2002. The red to near-infrared  
27 luminescence in alkali feldspar. Contributions to Mineralogy and Petrology 143, 484–494.  
28 doi: 10.1007/s00410-002-0359-4.
- 29 Buylaert, J.P., Jain, M., Murray, A.S., Thomsen, K.J., Lapp, T., 2012. IR-RF dating of sand-sized  
30 K-feldspar extracts: A test of accuracy. Radiation Measurements 47, 759–765. doi:  
31 10.1016/j.radmeas.2012.06.021.
- 32 Buylaert, J.P., Murray, A.S., Thomsen, K.J., Jain, M., 2009. Testing the potential of an elevated  
33 temperature IRSL signal from K-feldspar. Radiation Measurements 44, 560–565. doi:  
34 10.1016/j.radmeas.2009.02.007.

- 35 Clark, R.J., Bailiff, I.K., 1998. Fast time-resolved luminescence emission spectroscopy in some  
36 feldspars. *Radiation Measurements* 29, 553–560. doi: 10.1016/S1350-4487(98)00068-7.
- 37 Coussot, C., Liard, M., Kreutzer, S., Mercier, N., 2019. Séquence de Comblement d'un  
38 Paléovallon en Contexte de Plateau (290-10 Ka) : La Coupe De Courville-Sur-Eure (Eure-Et-  
39 Loir, France). *Quaternaire*, 167–183.
- 40 Degering, D., Krbetschek, M.R., 2007. Dating of interglacial sediments by luminescence methods,  
41 in: *The climate of past interglacials. Developments in Quaternary Sciences*. Elsevier, pp. 157–  
42 171. doi: 10.1016/S1571-0866(07)80036-4.
- 43 Duller, G.A.T., 1992. Luminescence chronology of raised marine terraces, South-West North  
44 Island, New Zealand. PhD thesis, University of Aberystwyth, UK, pp. 236.
- 45 Efron, B., 1979. Bootstrap Methods: Another Look at the Jackknife. *Ann. Statist.* 7, 1–26. doi:  
46 10.1214/aos/1176344552.
- 47 Eissmann, L., 2002. Quaternary geology of eastern Germany (Saxony, Saxon–Anhalt, South  
48 Brandenburg, Thüringia), type area of the Elsterian and Saalian Stages in Europe. *Quaternary  
49 Science Reviews* 21, 1275-1346. doi: 10.1016/S0277-3791(01)00075-0.
- 50 Erfurt, G., 2003a. Infrared luminescence of  $Pb^{+}$  centres in potassium-rich feldspars. *Physica status  
51 solidi (a)* 200, 429–438. doi: 10.1002/pssa.200306700.
- 52 Erfurt, G., 2003b. Radiolumineszenzspektroskopie und -dosimetrie an Feldspäten und  
53 synthetischen Luminophoren für die geochronometrische Anwendung. PhD thesis,  
54 Technische Universität Bergakademie Freiberg, Germany, pp. 141.
- 55 Erfurt, G., Krbetschek, M.R., 2003a. Studies on the physics of the infrared radioluminescence of  
56 potassium feldspar and on the methodology of its application to sediment dating. *Radiation  
57 Measurements* 37, 505–510. doi: 10.1016/S1350-4487(03)00058-1.
- 58 Erfurt, G., Krbetschek, M.R., 2003b. IRSAR - A single-aliquot regenerative-dose dating protocol  
59 applied to the infrared radiofluorescence (IR-RF) of coarse-grain K-feldspar. *Ancient TL* 21,  
60 35–42.

- 61 Erfurt, G., Krbetschek, M.R., Bortolot, V.J., Preusser, F., 2003. A fully automated multi-spectral  
62 radioluminescence reading system for geochronometry and dosimetry. *Nuclear Instruments*  
63 *and Methods in Physics Research Section B: Beam Interactions with Materials and Atoms*  
64 207, 487–499. doi: 10.1016/S0168-583X(03)01121-2.
- 65 Finch, A.A., Klein, J., 1999. The causes and petrological significance of cathodoluminescence  
66 emissions from alkali feldspars. *Contributions to Mineralogy and Petrology* 135, 234–243.  
67 doi: 10.1007/s004100050509.
- 68 Frouin, M., 2014. Les feldspaths comme support pour la datation par luminescence de gisements  
69 archéologiques et de séquences quaternaires d’Aquitaine. PhD thesis, Université Bordeaux  
70 Montaigne, France, pp. 390.
- 71 Frouin, M., Huot, S., Kreutzer, S., Lahaye, C., Lamothe, M., Philippe, A., Mercier, N., 2017. An  
72 improved radiofluorescence single-aliquot regenerative dose protocol for K-feldspars.  
73 *Quaternary Geochronology* 38, 13–24. doi: 10.1016/j.quageo.2016.11.004.
- 74 Frouin, M., Huot, S., Mercier, N., Lahaye, C., Lamothe, M., 2015. The issue of laboratory  
75 bleaching in the infrared-radiofluorescence dating method. *Radiation Measurements* 81, 212–  
76 217. doi: 10.1016/j.radmeas.2014.12.012.
- 77 Fu, X., Zhang, J.-F., Zhou, L.-P., 2012. Comparison of the properties of various optically  
78 stimulated luminescence signals from potassium feldspar. *Radiation Measurements* 47, 210–  
79 218. doi:10.1016/j.radmeas.2011.12.007
- 80 Garcia-Guinea, J., Townsend, P.D., Sanchez-Muñoz, L., Rojo, J.M., 1999. Ultraviolet-blue ionic  
81 luminescence of alkali feldspars from bulk and interfaces. *Physics and Chemistry of Minerals*  
82 26, 658–667. doi: 10.1007/s002690050231.
- 83 Geake, J.E., Walker, G., Telfer, D.J., Mills, A.A., 1977. The cause and significance of  
84 luminescence in lunar plagioclase. *Philosophical Transactions of the Royal Society A:*  
85 *Mathematical, Physical and Engineering Sciences* 285, 403–408. doi: 10.1098/rsta.1977.0081.

- 86 Gorobets, B.S., Portnov, A.M., Rogozhin, A.A., 1995. Luminescence spectroscopy of the earth.  
87 Radiation Measurements 24, 485–491. doi: 10.1016/1350-4487(94)00124-J.
- 88 Guérin, G., Valladas, G., 1980. Thermoluminescence dating of volcanic plagioclases. Nature 286,  
89 697–699. doi: 10.1038/286697a0.
- 90 Herber, L.J., 1969. Separation of Feldspar from Quartz by Flotation. The American Mineralogist  
91 54, 1212–1215.
- 92 Hetzel, R., Tao, M., Niedermann, S., Strecker, M.R., Ivy-Ochs, S., Kubik, P.W., Gao, B., 2004.  
93 Implications of the fault scaling law for the growth of topography: mountain ranges in the  
94 broken foreland of north-east Tibet. Terra Nova 16, 157–162. doi:10.1111/j.1365-  
95 3121.2004.00549.x
- 96 Heydari, M., Guérin, G., Zeidi, M., Conard, N. J., 2021. Bayesian luminescence dating at Ghār-e  
97 Boof, Iran, provides a new chronology for Middle and Upper Paleolithic in the southern Zagro.  
98 Journal of Human Evolution 151, 102926. doi:10.1016/j.jhevol.2020.102926
- 99 Huntley, D.J., 2006. An explanation of the power-law decay of luminescence. J. Phys.: Condens.  
100 Matter 18, 1359–1365. doi: 10.1088/0953-8984/18/4/020.
- 101 Huntley, D.J., Godfrey-Smith, D., Thewalt, M., 1985. Optical dating of sediments. Nature 14, 27-  
102 33. <https://doi.org/10.1038/313105a0>.
- 103 Huntley, D.J., Lamothe, M., 2001. Ubiquity of anomalous fading in K-feldspars and the  
104 measurement and correction for it in optical dating. Canadian Journal of Earth Sciences 38,  
105 1093–1106. doi: 10.1139/cjes-38-7-1093.
- 106 Huntley, D.J., Lian, O.B., 2006. Some observations on tunnelling of trapped electrons in feldspars  
107 and their implications for optical dating. Quaternary Science Reviews 25, 2503–2512. doi:  
108 [10.1016/j.quascirev.2005.05.011](https://doi.org/10.1016/j.quascirev.2005.05.011).
- 109 Hütt, G., Jaek, I., Tchonka, J., 1988. Optical dating: K-Feldspars optical response stimulation  
110 spectra. Quaternary Science Reviews 7, 381–385. doi: 10.1016/0277-3791(88)90033-9.

- 111 Huot, S., Frouin, M., Lamothe, M., 2015. Evidence of shallow TL peak contributions in infrared  
112 radiofluorescence. *Radiation Measurements* 81, 237–241. doi:  
113 10.1016/j.radmeas.2015.05.009.
- 114 Jain, M., Ankjærgaard, C., 2011. Towards a non-fading signal in feldspar: Insight into charge  
115 transport and tunnelling from time-resolved optically stimulated luminescence. *Radiation*  
116 *Measurements* 46, 292–309. doi: 10.1016/j.radmeas.2010.12.004.
- 117 Kadereit, A., Kühn, P., Wagner, G.A., 2010. Holocene relief and soil changes in loess-covered  
118 areas of south-western Germany: The pedosedimentary archives of Bretten-Bauerbach  
119 (Kraichgau). *Quaternary International* 222, 96–119. doi: 10.1016/j.quaint.2009.06.025.
- 120 Kars, R.H., Wallinga, J., 2009. IRSL dating of K-feldspars: Modelling natural dose response  
121 curves to deal with anomalous fading and trap competition. *Radiation Measurements* 44, 594–  
122 599.
- 123 Klasens, H.A., 1946. Transfer of energy between centres in zinc sulphide phosphors. *Nature* 158,  
124 306–307. doi: 10.1038/158306c0.
- 125 Krbetschek, M.R., Götze, J., Irmer, G., Rieser, U., Trautmann, T., 2002. The red luminescence  
126 emission of feldspar and its wavelength dependence on K, Na, Ca  $\pm$  composition. *Mineralogy*  
127 *and Petrology* 76, 167–177. doi:10.1007/s007100200039
- 128 Krbetschek, M.R., Degering, D., Alexowsky, W., 2008. Infrarot-Radiofluoreszenz-Alter (IR-RF)  
129 unter-saalezeitlicher Sedimente Mittel- und Ostdeutschlands. *Zeitschrift der Deutschen*  
130 *Gesellschaft für Geowissenschaften* 159, 133–140. doi: 10.1127/1860-1804/2008/0159-0133.
- 131 Krbetschek, M.R., Götze, J.U., Dietrich, A., Trautmann, T., 1997. Spectral information from  
132 minerals relevant for luminescence dating. *Radiation Measurements* 27, 695–748. doi:  
133 10.1016/S1350-4487(97)00223-0.
- 134 Krbetschek, M.R., Rieser, U., 1995. Luminescence spectra of alkali feldspars and plagioclases.  
135 *Radiation Measurements* 24, 473–477. doi: 10.1016/1350-4487(95)00011-3.

- 136 Krbetschek, M.R., Trautmann, T., 2000. A spectral radioluminescence study for dating and  
137 dosimetry. *Radiation Measurements* 32, 853–857. doi: 10.1016/S1350-4487(00)00085-8.
- 138 Krbetschek, M.R., Trautmann, T., Dietrich, A., Stolz, W., 2000. Radioluminescence dating of  
139 sediments: methodological aspects. *Radiation Measurements* 32, 493–498. doi:  
140 10.1016/S1350-4487(00)00122-0.
- 141 Krbetschek, M.R., Erfurt, G., Degering, D. 2003. *Radiofluorescence dating: A novel method for*  
142 *age determination of clastic sediment deposits from about 20 ka to 300 ka.* Poster presentation;  
143 XVI Inqua Congress, Reno (USA).
- 144 Kreutzer, S., Duval, M., Bartz, M., Bertran, P., Bosq, M., Eynaud, F., Verdin, F., Mercier, N.,  
145 2018a. Deciphering long-term coastal dynamics using IR-RF and ESR dating: A case study  
146 from Médoc, south-west France. *Quaternary Geochronology* 48, 108–120. doi:  
147 10.1016/j.quageo.2018.09.005.
- 148 Kreutzer, S., Lauer, T., Meszner, S., Krbetschek, M.R., Faust, D., Fuchs, M., 2014. Chronology of  
149 the Quaternary profile Zeuchfeld in Saxony-Anhalt / Germany – a preliminary luminescence  
150 dating study. *Zeitschrift für Geomorphologie* 58, 5–26. doi: 10.1127/0372-8854/2012/S-  
151 00112.
- 152 Kreutzer, S., Martin, L., Dubernet, S., Mercier, N., 2018b. The IR-RF alpha-Efficiency of K-  
153 feldspar. *Radiation Measurements* 120, 148–156. doi: 10.1016/j.radmeas.2018.04.019.
- 154 Kreutzer, S., Burow, C., Dietze, M., Fuchs, M., Schmidt, C., Fischer, M., Friedrich, J., 2018c.  
155 Luminescence: Comprehensive Luminescence Dating Data Analysis. R package version 0.8.6,  
156 <https://CRAN.R-project.org/package=Luminescence>.
- 157 Kreutzer, S., Murari, M.K., Frouin, M., Fuchs, M., Mercier, N., 2017. Always remain suspicious:  
158 a case study on tracking down a technical artefact while measuring IR-RF. *Ancient TL* 35,  
159 20–30.
- 160 Kreutzer, S., Schmidt, C., Fuchs, M.C., Dietze, M., Fischer, M., Fuchs, M., 2012. Introducing an  
161 R package for luminescence dating analysis. *Ancient TL* 30, 1–8.

- 162 Kumar, R., Kook, M., Murray, A.S., Jain, M., 2018. Towards direct measurement of electrons in  
163 metastable states in K-feldspar: Do infrared-photoluminescence and radioluminescence probe  
164 the same trap? *Radiation Measurements* 120, 1–17. doi: [10.1016/j.radmeas.2018.06.018](https://doi.org/10.1016/j.radmeas.2018.06.018).
- 165 Kumar, R., Martin, L.I.D.J., Poelman, D., Vandenberghe, D., De Grave, J., Kook, M., Jain, M.,  
166 2020. Site-selective mapping of metastable states using electron-beam induced luminescence  
167 microscopy. *Sci Rep* 10, 1270–14. doi:10.1038/s41598-020-72334-7
- 168 Kumar, R., Kook, M., Jain, M., 2021. Sediment dating using Infrared Photoluminescence.  
169 *Quaternary Geochronology* 62, 101147. doi:10.1016/j.quageo.2020.101147
- 170 Lamothe, M., Auclair, M., Hamzaoui, C., Huot, S., 2003. Towards a prediction of long-term  
171 anomalous fading of feldspar IRSL. *Radiation Measurements* 37, 493–498.
- 172 Lamothe, M., Brisson, L.F., Hardy, F., 2020. Circumvention of anomalous fading in feldspar  
173 luminescence dating using Post-Isothermal IRSL. *Quaternary Geochronology* 57, 101062.  
174 doi:10.1016/j.quageo.2020.101062
- 175 Larsen, E., Johannessen, N.E., Kowalczyk, P.B., Kleiv, R.A., 2019. Selective flotation of K-  
176 feldspar from Na-feldspar in alkaline environment. *Minerals Engineering* 142, 105928.  
177 doi:10.1016/j.mineng.2019.105928
- 178 Lapp, T., Jain, M., Thomsen, K.J., Murray, A.S., Buylaert, J.P., 2012. New luminescence  
179 measurement facilities in retrospective dosimetry. *Radiation Measurements* 47, 803–808. doi:  
180 10.1016/j.radmeas.2012.02.006
- 181 Lauer, T., Krbetschek, M.R., Frechen, M., Tsukamoto, S., Hoselmann, C., Weidenfeller, M., 2011.  
182 Infrared radiofluorescence (IR-RF) dating of middle pleistocene fluvial archives of the  
183 Heidelberg Basin (Southwest Germany). *Geochronometria* 38, 23–33. doi: 10.2478/s13386-  
184 011-0006-9.
- 185 Lauer, T., Weiss, M., 2018. Timing of the Saalian- and Elsterian glacial cycles and the implications  
186 for Middle – Pleistocene hominin presence in central Europe. *Scientific Reports*, 8: 5111.  
187 <https://doi.org/10.1038/s41598-018-23541-w>.



- 188 Li, Y., Tsukamoto, S., Frechen, M., Gabriel, G., 2017. Timing of fluvial sedimentation in the  
189 Upper Rhine Graben since the Middle Pleistocene: constraints from quartz and feldspar  
190 luminescence dating. *Boreas* 47, 256–270. doi:10.1111/bor.12266
- 191 Li, B., Roberts, R.G., Jacobs, Z., Li, S.-H., 2014. A single-aliquot luminescence dating procedure  
192 for K-feldspar based on the dose-dependent MET-pIRIR signal sensitivity. *Quaternary*  
193 *Geochronology* 20, 51–64. doi:10.1016/j.quageo.2013.11.001
- 194 Li, B., Li, S.-H., 2013. The effect of band-tail states on the thermal stability of the infrared  
195 stimulated luminescence from K-feldspar. *Journal of Luminescence* 136, 5–10. doi:  
196 10.1016/j.jlumin.2012.08.043.
- 197 Li, B., Li, S.-H., 2011a. Luminescence dating of K-feldspar from sediments: A protocol without  
198 anomalous fading correction. *Quaternary Geochronology* 6, 468–479. doi:  
199 10.1016/j.quageo.2011.05.001.
- 200 Li, B., Li, S.-H., 2011b. Thermal stability of infrared stimulated luminescence of sedimentary K-  
201 feldspar. *Radiation Measurements* 46, 29–36. doi:10.1016/j.radmeas.2010.10.002
- 202 Liu, J., Murray, A.S., Buylaert, J.-P., Jain, M., Chen, J., Lu, Y., 2016. Stability of fine-grained TT-  
203 OSL and post-IR IRSL signals from a c. 1 Ma sequence of aeolian and lacustrine deposits  
204 from the Nihewan Basin (northern China). *Boreas* 45, 703–714. doi:10.1111/bor.12180
- 205 Lowick, S.E., Trauerstein, M., Preusser, F., 2012. Testing the application of post IR-IRSL dating  
206 to fine grain waterlain sediments. *Quaternary Geochronology* 8, 33-40. doi:  
207 10.1016/j.quageo.2011.12.003.
- 208 Lowick, S.E., Valla, P.G., 2018. Characterising the luminescence behaviour of 'infinitely old'  
209 quartz samples from Switzerland. *Quaternary Geochronology* 43, 1–11. doi:  
210 10.1016/j.quageo.2017.09.004.
- 211 Marfunin, A.S., Bershov, L.V., 1970. Paramagnetic in feldspars and their possible  
212 crystalchemical and petrological significance (ПАРАМАГНИТНЫЕ ЦЕНТРЫ В

- 213 ПОЛЕВЫХ ШПАТАХ И ИХ ВОЗМОЖНОЕ КРИСТАЛЛОХИМИЧЕСКОЕ  
214 И ПЕТРОГРАФИЧЕСКОЕ ЗНАЧЕНИЕ). Dokl. Akad. Nauk 193, 421–414.
- 215 Marfunin, A.S., 1979. Spectroscopy, luminescence and radiation centers in minerals. Springer  
216 Berlin Heidelberg. doi: 10.1007/978-3-642-67112-8.
- 217 Meszner, S., Kreutzer, S., Fuchs, M., Faust, D., 2013. Late Pleistocene landscape dynamics in  
218 Saxony, Germany: Paleoenvironmental reconstruction using loess-paleosol sequences.  
219 Quaternary International 296, 95–107. doi: 10.1016/j.quaint.2012.12.040.
- 220 Meyer, M.C., Austin, P., Tropper, P., 2013. Quantitative evaluation of mineral grains using  
221 automated SEM–EDS analysis and its application potential in optically stimulated  
222 luminescence dating. Radiation Measurements 58, 1–11. doi: 10.1016/j.radmeas.2013.07.004.
- 223 Miallier, D., Sanzelle, S., Fain, J., 1983. The use of flotation technique to separate quartz from  
224 feldspar. Ancient TL 5–6.
- 225 Mittelstrass, D., Kreutzer, S., preprint. Spatially Resolved Infrared Radiofluorescence: Single-  
226 grain K-feldspar Dating using CCD Imaging, Geochronology Discussion, 1-31. doi:  
227 10.5194/gchron-2020-43
- 228 Murari, M.K., Kreutzer, S., Fuchs, M., 2018. Further investigations on IR-RF: Dose recovery and  
229 correction. Radiation Measurements 120, 110–119. doi: 10.1016/j.radmeas.2018.04.017.
- 230 Murray, A.S., Buylaert, J.P., Thomsen, K.J., Jain, M., 2009. The effect of preheating on the IRSL  
231 signal from feldspar. Radiation Measurements 44, 554–559. doi:  
232 10.1016/j.radmeas.2009.02.004.
- 233 Murray, A.S., Wintle, A.G., 2000. Luminescence dating of quartz using an improved single-aliquot  
234 regenerative-dose protocol. Radiation Measurements 32, 57–73. doi: 10.1016/S1350-  
235 4487(99)00253-X.
- 236 Nagli, L.E., Dyachenko, S.V., 1988. Influence of a  $v_c^-$  vacancy on luminescence of  $Pb^+$  centres in  
237 alkali halides. Phys. stat. sol. (b) 146, 295–301. doi: 10.1002/pssb.2221460131.

- 238 Novothny, Á., Frechen, M., Horváth, E., Krbetschek, M.R., Tsukamoto, S., 2010. Infrared  
239 stimulated luminescence and radiofluorescence dating of aeolian sediments from Hungary.  
240 *Quaternary Geochronology* 5, 114–119. doi: 10.1016/j.quageo.2009.05.002.
- 241 Ostrooumov, M., 2016. *Amazonite*. Elsevier. doi: 10.1016/C2015-0-00152-6.
- 242 Pavesi, L., Ceschini, M., 1993. Stretched-exponential decay of the luminescence in porous silicon.  
243 *Physical Review B* 48, 17625–17628. doi: 10.1103/PhysRevB.48.17625.
- 244 Pagonis, V., Phan, H., Ruth, D., Kitis, G., 2013. Further investigations of tunneling recombination  
245 processes in random distributions of defects. *Radiation Measurements* 58, 66–74.  
246 doi:10.1016/j.radmeas.2013.08.006
- 247 Pagonis, V., Kulp, C., 2017. Monte Carlo simulations of tunneling phenomena and nearest  
248 neighbor hopping mechanism in feldspars. *Journal of Luminescence* 181, 114–120.  
249 doi:10.1016/j.jlumin.2016.09.014
- 250 Pagonis, V., Friedrich, J., Discher, M., Müller-Kirschbaum, A., Schlosser, V., Kreutzer, S., Chen,  
251 R., Schmidt, C., 2019. Excited state luminescence signals from a random distribution of  
252 defects: A new Monte Carlo simulation approach for feldspar. *Journal of Luminescence* 207,  
253 266–272. doi:10.1016/j.jlumin.2018.11.024
- 254 Poolton, N.R.J., Bøtter-Jensen, L., Johnsen, O., 1996. On the relationship between luminescence  
255 excitation spectra and feldspar mineralogy. *Radiation Measurements* 26, 93–101. doi:  
256 10.1016/1350-4487(95)00288-X.
- 257 Poolton, N.R.J., Bøtter-Jensen, L., Johnsen, O., 1995. Thermo-optical properties of optically  
258 stimulated luminescence in feldspars. *Radiation Measurements* 24, 531–534. doi:  
259 10.1016/1350-4487(94)00114-G.
- 260 Poolton, N.R.J., Kars, R.H., Wallinga, J., Bos, A.J.J., 2009. Direct evidence for the participation  
261 of band-tails and excited-state tunnelling in the luminescence of irradiated feldspars. *J. Phys.:*  
262 *Condens. Matter* 21, 485505. doi: 10.1088/0953-8984/21/48/485505.

- 263 Poolton, N.R.J., Mauz, B., Lang, A., Jain, M., Malins, A.E.R., 2006. Optical excitation processes  
264 in the near band-edge region of and feldspar. *Radiation Measurements* 41, 542–548. doi:  
265 10.1016/j.radmeas.2005.12.001.
- 266 Poolton, N.R.J., Ozanyan, K.B., Wallinga, J., Murray, A.S., Bøtter-Jensen, L., 2002a. Electrons in  
267 feldspar II: a consideration of the influence of conduction band-tail states on luminescence  
268 processes. *Physics and Chemistry of Minerals* 29, 217–225. doi: 10.1007/s00269-001-0218-  
269 2.
- 270 Poolton, N.R.J., Wallinga, J., Murray, A.S., Bulur, E., Bøtter-Jensen, L., 2002b. Electrons in  
271 feldspar I: on the wavefunction of electrons trapped at simple lattice defects. *Physics and*  
272 *Chemistry of Minerals* 29, 210–216. doi: 10.1007/s00269-001-0217-3.
- 273 Porat, N., Faerstein, G., Medialdea, A., Murray, A.S., 2015. Re-examination of common extraction  
274 and purification methods of quartz and feldspar for luminescence dating. *Ancient TL* 33, 22–  
275 30.
- 276 Prasad, A.K., 2017. Understanding defect related luminescence processes in wide bandgap  
277 materials using low temperature multi-spectroscopic techniques. PhD thesis, DTU Nutech,  
278 Denmark, pp. 196.
- 279 Prasad, A.K., Jain, M., 2018. Dynamics of the deep red Fe<sup>3+</sup> photoluminescence emission in  
280 feldspar. *Journal of Luminescence* 196, 462–469. doi: 10.1016/j.jlumin.2017.11.051.
- 281 Prasad, A.K., Poolton, N.R.J., Kook, M., Jain, M., 2017. Optical dating in a new light: A direct,  
282 non-destructive probe of trapped electrons. *Sci Rep* 7, 461. doi: 10.1038/s41598-017-10174-  
283 8.
- 284 Preusser, F., Degering, D., Fuchs, M., Hilgers, A., Kadereit, A., Klasen, N., Krbetschek, M.R.,  
285 Richter, D., Spencer, J.Q.G., 2008. Luminescence dating: basics, methods and applications.  
286 *Eiszeitalter und Gegenwart (Quaternary Science Journal)* 57, 95–149. doi: 10.3285/eg.57.1-  
287 2.5.

- 288 Prescott, J.R., Huntley, D.J., Hutton, J.T., 1993. Estimation of equivalent dose in  
289 thermoluminescence dating - the *Australian slide* method. *Ancient TL* 11, 1–5.
- 290 R Core Team, 2018. R: A Language and Environment for Statistical Computing. R Foundation for  
291 Statistical Computing, Vienna, Austria. <https://r-project.org>.
- 292 Qin, J., Chen, J., Li, Y., Zhou, L., 2018. Initial sensitivity change of K-feldspar pIRIR signals due  
293 to uncompensated decrease in electron trapping probability: Evidence from radiofluorescence  
294 measurements. *Radiation Measurements* 120, 131–136. doi:10.1016/j.radmeas.2018.06.017
- 295 Richter, D., Pintaske, R., Dornich, K., Krbetschek, M.R., 2012. A novel beta source design for  
296 uniform irradiation in dosimetric applications. *Ancient TL* 30, 57–63.
- 297 Richter, D., Richter, A., Dornich, K., 2013. lexsyg — a new system for luminescence research.  
298 *Geochronometria* 40, 220–228. doi: 10.2478/s13386-013-0110-0.
- 299 Rieser, U., Habermann, J., Wagner, G.A., 1999. Luminescence dating: A new high sensitivity  
300 TL/OSL emission spectrometer. *Quaternary Science Reviews* 18, 311–315. doi:  
301 10.1016/S0277-3791(98)00064-X.
- 302 Rieser, U., Hütt, G., Krbetschek, M.R., Stolz, W., 1997. Feldspar IRSL emission spectra at high  
303 and low temperatures. *Radiation Measurements* 27, 273–278. doi: 10.1016/S1350-  
304 4487(96)00108-4.
- 305 Rieser, U., Krbetschek, M.R., Stolz, W., 1994. CCD-camera based high sensitivity TL/OSL-  
306 spectrometer. *Radiation Measurements* 23, 523–528. doi: 10.1016/1350-4487(94)90092-2.
- 307 Scerri, E.M.L., Shipton, C., Clark-Balzan, L., Frouin, M., Schwenninger, J.-L., Groucutt, H.S.,  
308 Breeze, P.S., Parton, A., Blinkhorn, J., Drake, N.A., Jennings, R., Cuthbertson, P., Omari,  
309 A.A., Alsharekh, A.M., Petraglia, M.D., 2018. The expansion of later Acheulean hominins  
310 into the Arabian Peninsula. *Scientific Reports* 8, 17165. doi: 10.1038/s41598-018-35242-5.
- 311 Schaarschmidt, M., Fu, X., Li, B., Ben Marwick, Khaing, K., Douka, K., Roberts, R.G., 2019.  
312 pIRIR and IR-RF dating of archaeological deposits at Badahlin and Gu Myaung Caves – First  
313 luminescence ages for Myanmar. *Quaternary Geochronology* 49, 262–270.

- 314 doi:10.1016/j.quageo.2018.01.001
- 315 Schäfer, J., Laurat, T., Kegler, J. F., 2003. Bericht zu den Ausgrabungen am altsteinzeitlichen  
316 Fundplatz Markkleeberg 1999 bis 2001. Arbeits- und Forschungsberichte zur sächsischen  
317 Bodendenkmalpfl. 45, 13–47.
- 318 Schilles, T., 2002. Die Infrarot-Radiolumineszenz von Feldspäten und ihr Einsatz in der  
319 Lumineszenzdatierung. PhD thesis, Ruprechts-Karls-Universität Heidelberg, Germany, pp.  
320 149.
- 321 Schilles, T., Habermann, J., 2000. Radioluminescence dating: the IR emission of feldspar.  
322 Radiation Measurements 32, 679–683. doi: 10.1016/S1350-4487(00)00081-0.
- 323 Schmidt, C., Kreutzer, S., DeWitt, R., Fuchs, M., 2015. Radiofluorescence of quartz: A review.  
324 Quaternary Geochronology 27, 66–77. doi: 10.1016/j.quageo.2015.01.005.
- 325 Schön, M., 1942. Zum Leuchtmechanismus der Kristallphosphore. Zeitschrift für Physik 119,  
326 463–471. doi: 10.1007/BF01339783.
- 327 Speit, B., Lehmann, G., 1982. Radiation defects in feldspars. Physics and Chemistry of Minerals  
328 8, 77–82. doi: [10.1007/BF00309017](https://doi.org/10.1007/BF00309017).
- 329 Spooner, N.A., 1992. Optical dating: Preliminary results on the anomalous fading of luminescence  
330 from feldspars. Quaternary Science Reviews 11, 139–145.  
331 doi:10.1016/0277-3791(92)90055-D
- 332 Sulaymonova, V.A., Fuchs, M.C., Gloaguen, R., Möckel, R., Merchel, S., Rudolph, M.,  
333 Krbetschek, M.R., 2018. Feldspar flotation as a quartz-purification method in cosmogenic  
334 nuclide dating: A case study of fluvial sediments from the Pamir. MethodsX 5, 717–726.  
335 doi:10.1016/j.mex.2018.06.014
- 336 Telfer, D.J., Walker, G., 1975. Optical detection of Fe<sup>3+</sup> in lunar plagioclase. Nature 258, 694–  
337 695. doi: 10.1038/258694a0.

- 338 Thomsen, K.J., Murray, A.S., Jain, M., Bøtter-Jensen, L., 2008. Laboratory fading rates of various  
339 luminescence signals from feldspar-rich sediment extracts. *Radiation Measurements* 43,  
340 1474–1486. doi: 10.1016/j.radmeas.2008.06.002.
- 341 Thomsen, K., Murray, A., Jain, M., 2010. Stability of IRSL signals from sedimentary K-feldspar  
342 samples. *Geochronometria* 38, 1–13. doi:10.2478/s13386-011-0003-z
- 343 Toyoda, S., Voinchet, P., Falguères, C., Dolo, J.M., Laurent, M., 2000. Bleaching of ESR signals  
344 by the sunlight: a laboratory experiment for establishing the ESR dating of sediments. *Applied*  
345 *Radiation and Isotopes* 52, 1357–1362. doi: 10.1016/S0969-8043(00)00095-6.
- 346 Trautmann, T., 1999. Radiolumineszenzuntersuchungen an Feldspat. PhD thesis, Technische  
347 Bergakademie Freiberg, Germany, pp. 99.
- 348 Trautmann, T., 2000. A study of radioluminescence kinetics of natural feldspar dosimeters:  
349 experiments and simulations. *Journal of Physics D: Applied Physics* 33, 2304–2310. doi:  
350 10.1088/0022-3727/33/18/315.
- 351 Trautmann, T., Krbetschek, M.R., Dietrich, A., Stolz, W., 2000a. The basic principle of  
352 radioluminescence dating and a localized transition model. *Radiation Measurements* 32, 487–  
353 492. doi: 10.1016/S1350-4487(00)00119-0.
- 354 Trautmann, T., Krbetschek, M.R., Dietrich, A., Stolz, W., 1999a. Feldspar radioluminescence: a  
355 new dating method and its physical background. *Journal of Luminescence* 85, 45–58. [https://](https://doi.org/10.1016/S0022-2313(99)00152-0)  
356 doi:10.1016/S0022-2313(99)00152-0.
- 357 Trautmann, T., Dietrich, A., Stolz, W., Krbetschek, M.R., 1999b. Radioluminescence Dating: A  
358 New Tool for Quaternary Geology and Archaeology. *Naturwissenschaften* 86, 441–444.  
359 doi:10.1007/s001140050649
- 360 Trautmann, T., Krbetschek, M.R., Dietrich, A., Stolz, W., 1998. Investigations of feldspar  
361 radioluminescence: potential for a new dating technique. *Radiation Measurements* 29, 421–  
362 425. doi: 10.1016/S1350-4487(98)00012-2.

- 363 Trautmann, T., Krbetschek, M.R., Stolz, W., 2000b. A systematic study of the radioluminescence  
364 properties of single feldspar grains. *Radiation Measurements* 32, 685–690. doi:  
365 10.1016/S1350-4487(00)00077-9.
- 366 Tsukamoto, S., Jain, M., Murray, A., Thiel, C., Schmidt, E., Wacha, L., Dohrmann, R., Frechen,  
367 M., 2012. A comparative study of the luminescence characteristics of polymineral fine grains  
368 and coarse-grained K-, and Na-rich feldspars. *Radiation Measurements* 47, 903-908. [https://](https://doi.org/10.1016/j.radmeas.2012.02.017)  
369 doi:10.1016/j.radmeas.2012.02.017.
- 370 Valladas, H., Valladas, G., 1982. Effet de l'irradiation alpha sur des grains de quartz. *PACT* 6,  
371 171–178.
- 372 Varma, V., Biswas, R.H., Singhvi, A.K., 2013. Aspects of infrared radioluminescence dosimetry  
373 in K-feldspar. *Geochronometria* 40, 266–273. doi: 10.2478/s13386-013-0125-6.
- 374 Visocekas, R., 1993. Tunneling radiative recombination in K-feldspar sanidine. *Nuclear Tracks*  
375 *and Radiation Measurements* 21, 175–178. doi: 10.1016/1359-0189(93)90073-I.
- 376 Wagner, G.A., Krbetschek, M.R., Degering, D., Bahain, J.J., Shao, Q., Falguères, C., Voinchet,  
377 P., Dolo, J.M., Garcia, T., Rightmire, G.P., 2010. Radiometric dating of the type-site for *Homo*  
378 *heidelbergensis* at Mauer, Germany. *Proceedings of the National Academy of Sciences* 107,  
379 19726–19730. doi: 10.1073/pnas.1012722107.
- 380 Wallinga, J., Murray, A., Wintle, A., 2000. The single-aliquot regenerative-dose (SAR) protocol  
381 applied to coarse-grain feldspar. *Radiation Measurements* 32, 529-533. doi: [10.1016/S1350-](https://doi.org/10.1016/S1350-4487(00)00091-3)  
382 [4487\(00\)00091-3](https://doi.org/10.1016/S1350-4487(00)00091-3)
- 383 White, W.B., Matsumura, M., Linnehan, D.G., Furukawa, T., Chandrasekhar, B.K., 1986.  
384 Absorption and luminescence of Fe<sup>3+</sup> in single-crystal orthoclase. *American Mineralogist* 71,  
385 1415–1419.
- 386 Wintle, A.G., 1973. Anomalous fading of thermoluminescence in mineral samples. *Nature* 245,  
387 143–144. <https://doi.org/10.1038/245143a0>.



- 388 Wintle, A.G., Murray, A.S., 2006. A review of quartz optically stimulated luminescence  
389 characteristics and their relevance in single-aliquot regeneration dating protocols. *Radiation*  
390 *Measurements* 41, 369–391. [doi: 10.1016/j.radmeas.2005.11.001](https://doi.org/10.1016/j.radmeas.2005.11.001).
- 391 Wintle, A.G., Adamiec, G., 2017. Optically stimulated luminescence signals from quartz: A  
392 review. *Radiation Measurements* 98, 10–33. doi:10.1016/j.radmeas.2017.02.003
- 393 Wünnemann, B., Hartmann, K., Altmann, N., Hambach, U., Pachur, H.-J., Zhang, H., 2007. 22.  
394 Interglacial and Glacial Fingerprints from Lake Deposits in the Gobi Desert, NW China. In:  
395 Sirocko, F., Claussen, M., Goni, M.F.S., Litt, T. (Eds.), 2007. *The Climate of Past*  
396 *Interglacials*. Elsevier., 323–347
- 397 Zhang, J., Li, S.-H., 2020. Review of the Post-IR IRSL Dating Protocols of K-Feldspar. *MPs* 3, 7–  
398 19. doi:10.3390/mps3010007

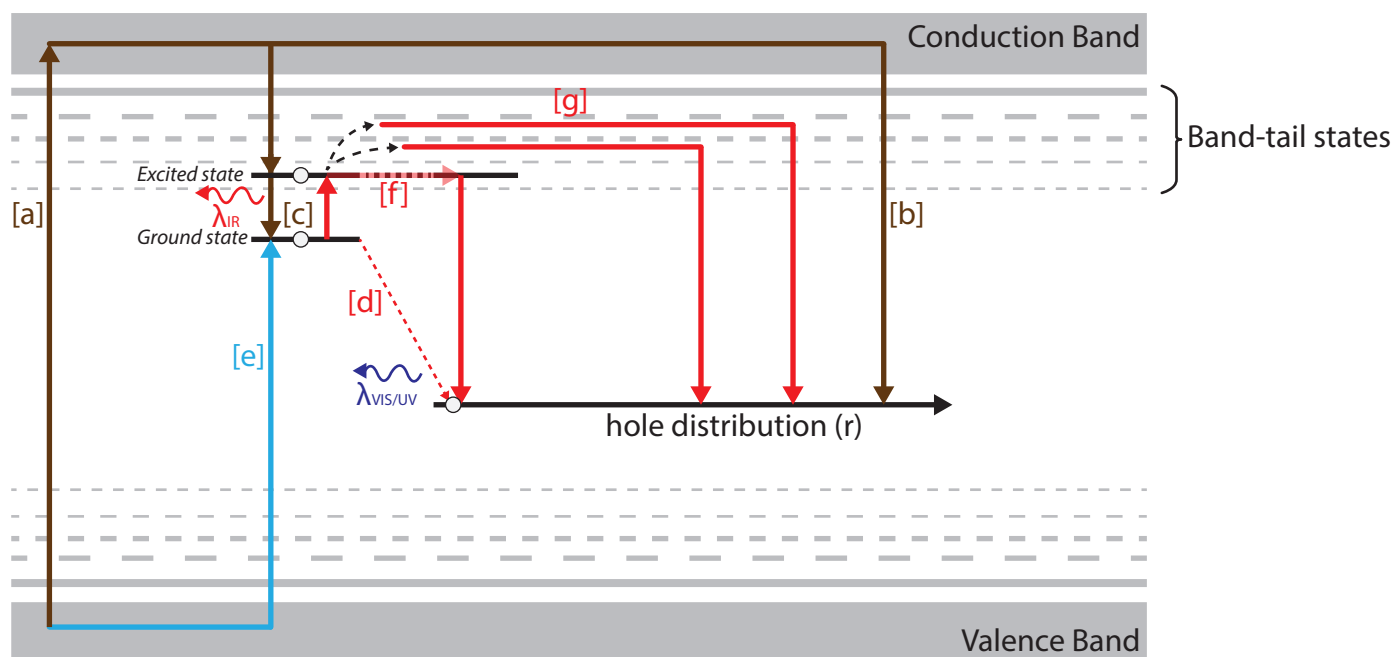
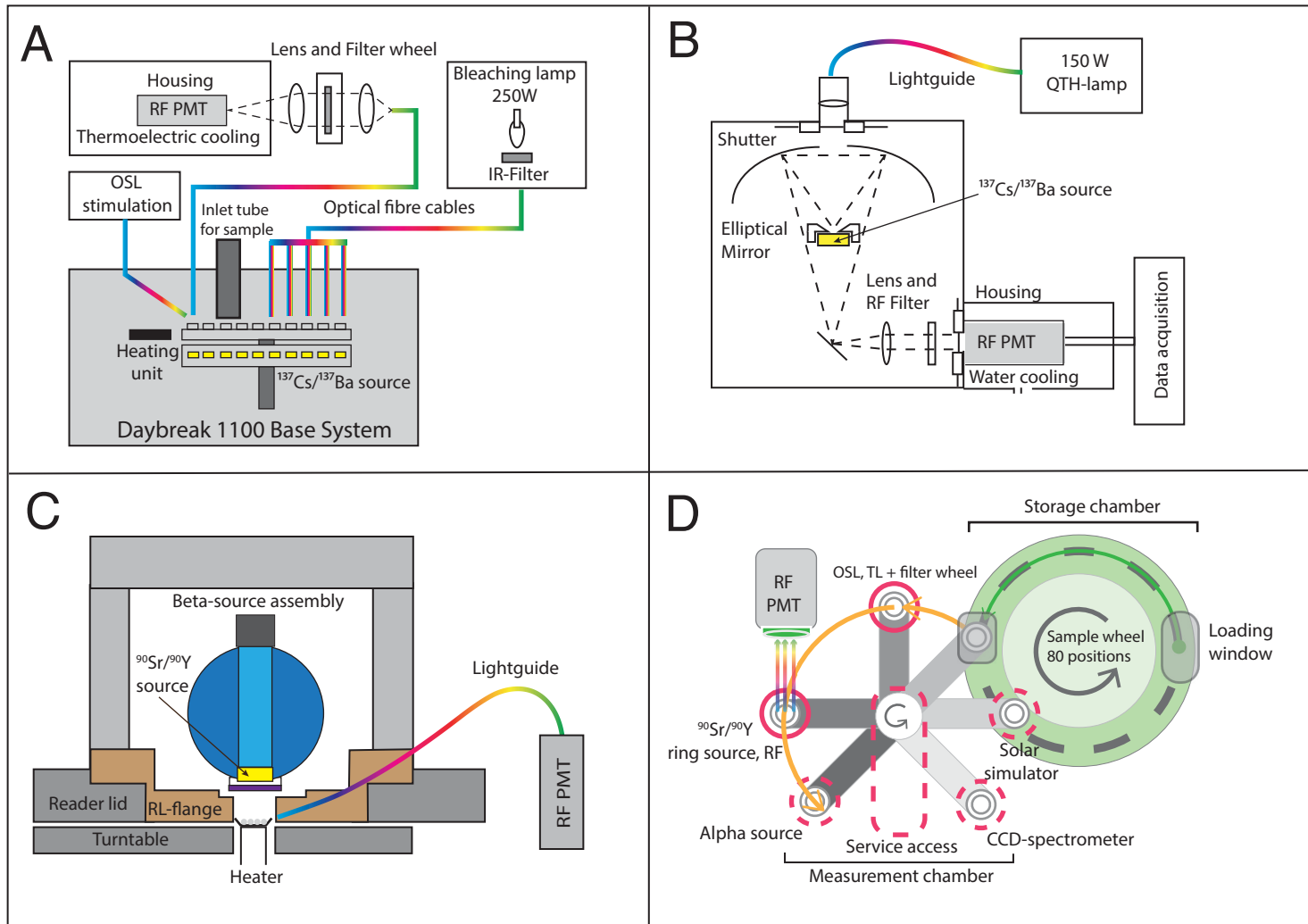
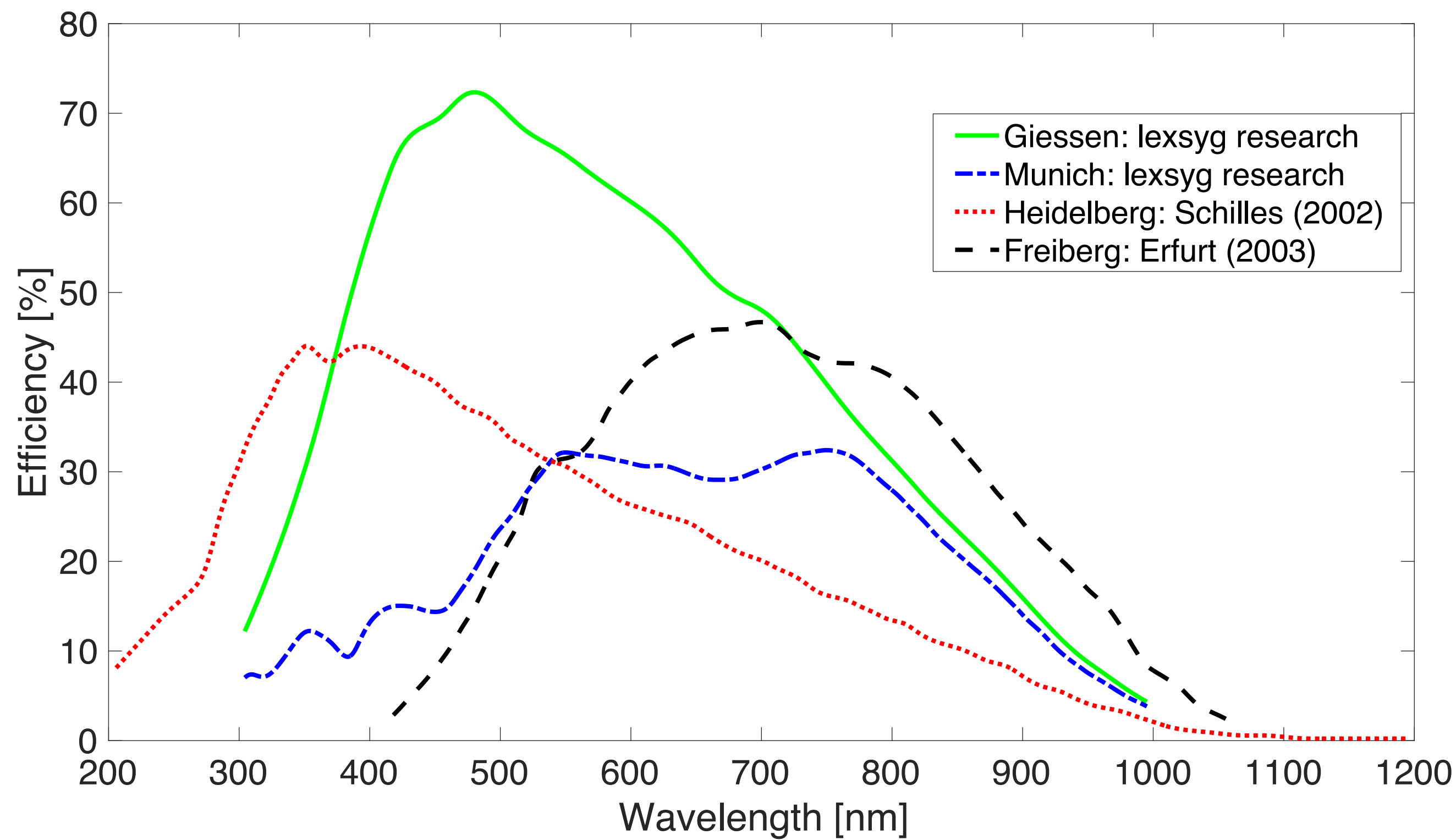


Figure 2

[Click here to access/download;Figure;Figure2\\_new.pdf](#)




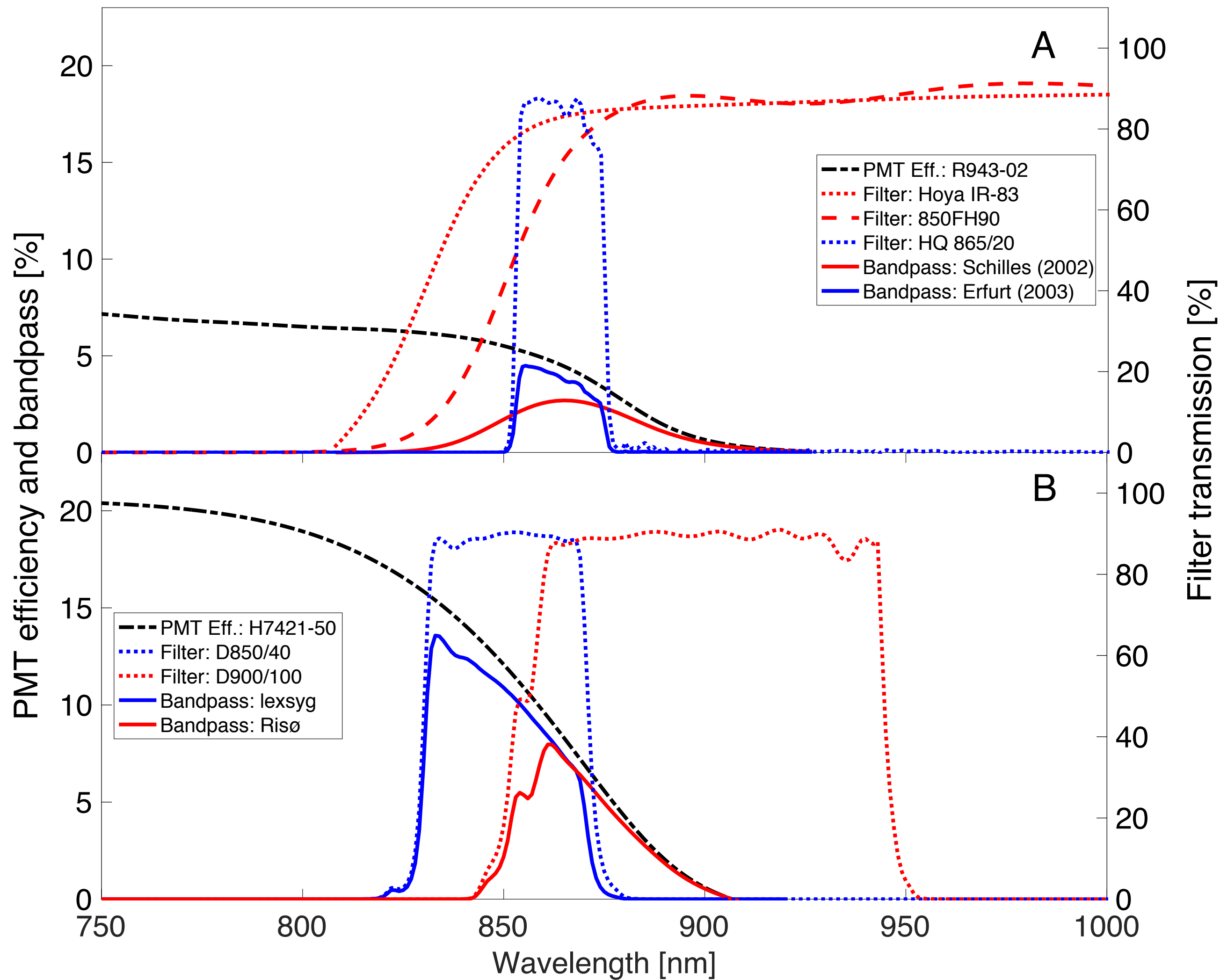
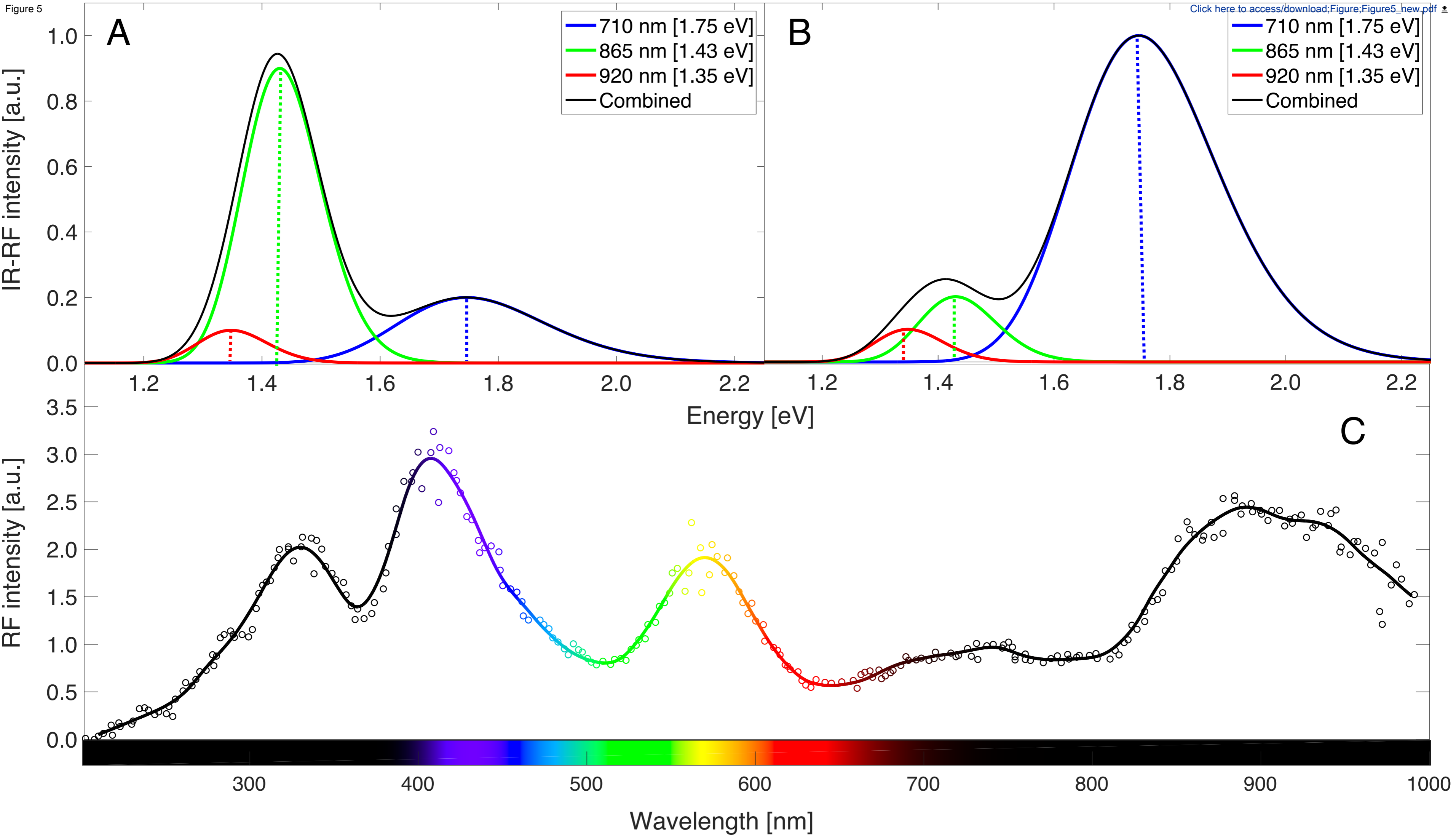


Figure 5



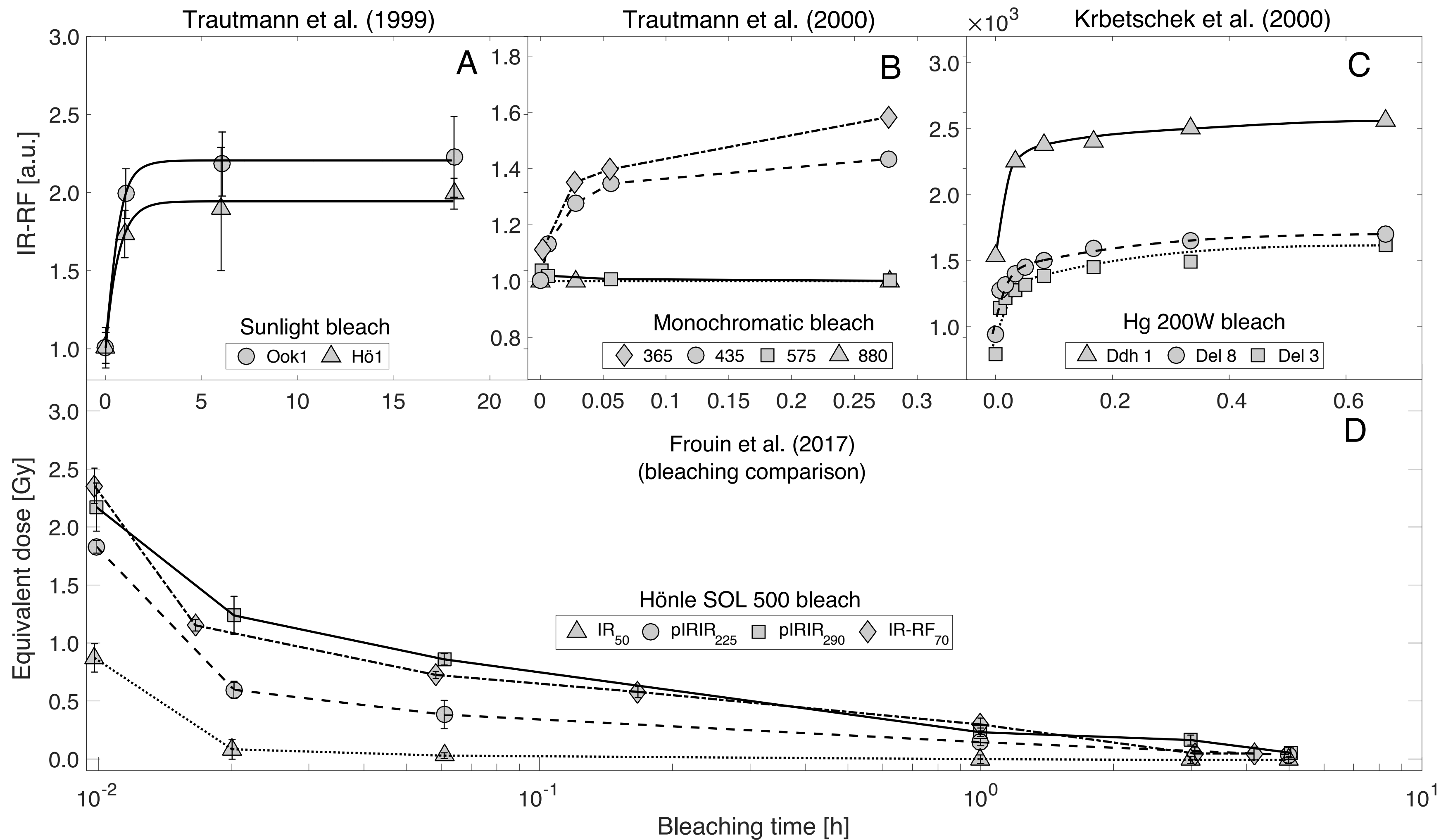
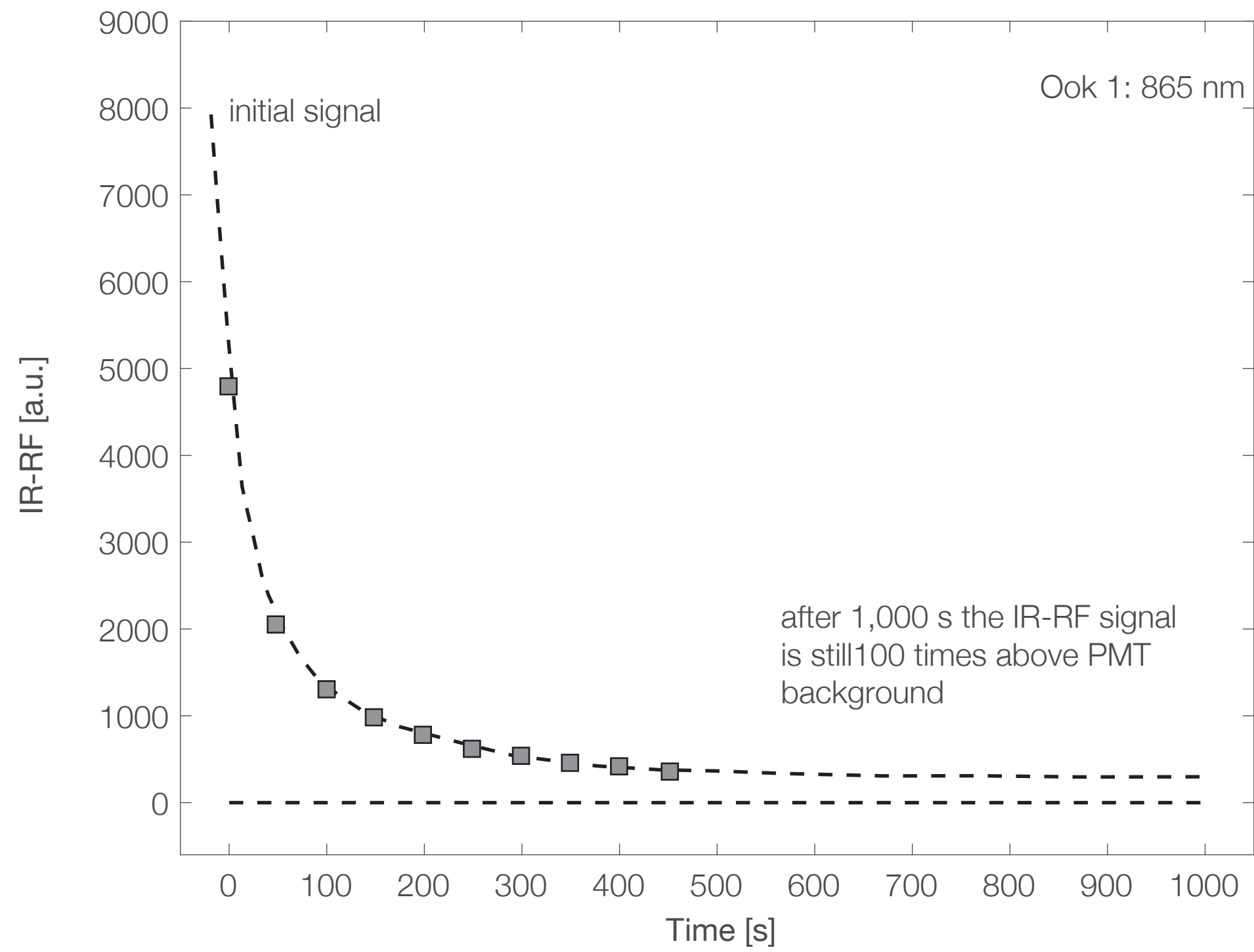


Figure 7





## Sensitivity I Schilles (2002)

## Sensitivity I Varma et al. (2013)

## Sensitivity I Murari et al. (2018)

IR-RF [a.u.]

